Pathogen Detection Technique using Nuclear Magnetic Resonance

by

Daniel Slater

A thesis submitted to the Graduate Faculty of
Auburn University
in partial fulfillment of the
requirements for the Degree of
Master of Science

Auburn, Alabama
May 5, 2013

Keywords: NMR Relaxation, Biosensor, MRI
Nanotechnology, Nanoparticles, Superparamagnetic

Copyright 2013 by Daniel Slater

Approved by

Barton C. Prorok, Chair, Associate Professor of Materials Engineering
Dong-Joo Kim, Associate Professor of Materials Engineering
Ron Beyers, MR Physicist and Safety Officer

Abstract

Nuclear Magnetic Resonance (NMR) signal relaxation is influenced by aggregate formation when magnetic nanoparticles bind with target molecules. In this study, a magnetic resonance based nanosensor was developed for a clinical MRI system. The goal of this research was the detection of target polystyrene microspheres conjugation with superparamagnetic iron oxide (SPIO) nanoparticles in a rapid and highly sensitive multiplexed fashion. The binding effects would occur due to the interaction of the streptavidin coated SPIO nanoparticles with the biotinylated polystyrene microspheres (BPM). The SPIO nanoparticles were used as a proximity sensor that would augment molecular interactions. The T_2 dephasing rate of nearby water molecule protons was demonstrated to be lower in the dispersed state rather than once aggregated thus providing an adjustment in transverse relaxation time, ΔT_2. An optimal concentration range of the SPIO nanoparticles was shown for its greatest sensitivity at affecting T_2 with any modification in the nanoparticles dispersion. By utilizing the optimal SPIO concentration, a NMR based nanosensor was developed that would identify the presence of the BPM within a solution. The SPIO nanoparticle sensor shows promise for its diagnostic capability and its portability.

Acknowledgments

I would like to thank Dr. Prorok for giving me the opportunity to work on this project and for his continuous support. I would also like to thank Dr. Ron Beyers from the Auburn MRI Center for his patient involvement with the MRI data collection and reduction. I also want to thank Marrianne Sullivan and Naveed Sidiqui for their assistance with supportive ideas and their suggested improvements. Finally, I want to thank all my committee members for their guidance throughout this research.

Table of Contents

Abstract ii

Acknowledgments iii

List of Tables vi

List of Figures vii

List of Abbreviations ix

Chapter 1 Introduction 1

1.1 Synopsis 1

1.2 Thesis Structure 6

Chapter 2 Literature Review 8

2.1 SPIO Nanoparticles 8

2.1a Comparison Between SPIO Nanoparticle Core Sizes 9

2.2b SPIO Nanoparticle Stability and Compatibility 10

2.2 Detection Mechanism 12

2.3 Differences between NMR Diagnostic Platforms 16

Chapter 3 Experimental Setup 22

3.1 Longitudinal Recovery (T_1) Parameters 22

3.2 Transverse Relaxation (T_2) Parameters 23

3.3 Magnetic Inhomogeniety Factor (T_2*) Parameters 23

3.4 Data Reduction 24

3.5 SEM 24

Chapter 4 Test Procedures 25

4.1 Test One: Relaxation Time Dependence on SPIO nanoparticle Concentration 25

4.2 Test Two: T_2* Minimum SPIO Nanoparticle Concentration Detection.....28

4.3 Test Three: Validity and Reliability of T_2 and T_2* 30

4.4 Test Four: T_2 as a Detection Mechanism.....31

4.5 Test Five: Detection at a Higher SPIO Nanoparticle Concentration 34

4.6 Test Six: Confirmation of T_2 Values with Increasing BPM Concentration 35

4.7 Test Seven: Determining Particle Settling Using Sagittal Imaging.....36

Chapter 5 Results and Discussions 39

5.1 Relaxation Time and Particle Core Size Comparison.....39

5.2 Reliability of T_2 and T_2* 41

5.3 Optimal SPIO Nanoparticle Concentration for T_2 Target Detection.....47

5.4 Detection of Polystyrene Microspheres (BPM).....49

Chapter 6 Conclusion.....55

Appendix 57

References 64

List of Tables

Table 2.1 Proton Relaxivity Data for Different SPIO Particle Core Sizes and Coatings 12

Table 3.1 T_1 Inversion Times 23

Table 3.2 T_2 Echo Times 23

Table 3.3 T_2* Echo Times 24

Table 4.1 MRI Testing Procedures 25

Table 4.2 Sample 79 and 80 SPIO molar concentration 32

Table 5.1 Wet-to-Dry Percentage Change in T_2* 44

Table 5.2 Reliability of T_2 and T_2* 47

Table 5.3 External Magnetic Fields Effect on T_2 for Equal Molar SPIO Samples 51

Table 7.1 Samples used for Test One with their respective SPIO core size and molar concentration 57

Table 7.2 Relaxation rates of each sample in Test One 58

Table 7.3 Test Two Samples with their respective SPIO molar concentration. 58

Table 7.4 Test Three Samples with their respective SPIO molar concentration. 59

Table 7.5 Test Four Samples with their respective SPIO and BPM concentration 60

Table 7.6 Test Five Samples with their respective SPIO and BPM concentration 61

Table 7.7 Test Six Samples with their respective SPIO and BPM concentration 61

Table 7.8 Refitted Test One Sample Concentration Values 63

List of Figures

Figure 1.1 Schematic of Proton Spins Aligning to Magnetic Field 2

Figure 1.2 Schematic of T_2 and T_2* decay 5

Figure 2.1 Availability of Differing Particle Sizes to Attach to Target Particles 10

Figure 2.2 Dependency of Proton Relaxation Rate on MNP Coatings and Core Sizes 11

Figure 2.3 Effects of Dispersed and Clustered MNPs on Surrounding Water Molecules 13

Figure 2.4 Change in T_2 due to MNP-Target Dissasembly 14

Figure 2.5 Selectivity of MNP Sensors 15

Figure 2.6 Image of an MRI 17

Figure 2.7 Images of a NMR Systems Schematic Diagram, Microcoil, and Microfluidic Network 18

Figure 2.8 Expected Change in T_2 with Increasing Target Concentrations 20

Figure 4.1 Image of Test Tube Rack Used for Tests One through Seven 26

Figure 4.2 Test One sample's SPIO nanoparticles molar quantities 27

Figure 4.3 SEM Images of the 30nm SPIO particles 28

Figure 4.4 Test Two sample's SPIO nanoparticles molar quantities 29

Figure 4.5 MR Image of Test Samples in Rack during Testing Procedures 29

Figure 4.6 Test Three sample's SPIO nanoparticles molar quantities 30

Figure 4.7 Diagram Indicating Predicated Changes in T_2 at SPIO Optimal Concentration 32

Figure 4.8 Image of Expected Binding Interaction between SPIO and BPM Molecules 33

Figure 4.9 Polystyrene microsphere count with its respective SPIO optimal concentration 34

Figure 4.10 Polystyrene microsphere samples combined with SPIO optimal concentration 35

Figure 4.11 Reimaged Test Five sample microsphere quantity to verify the repeatability of their T_2 values 36

Figure 4.12 MR Image of Test Seven Sagittal Slice 37

Figure 4.13 Location of Each Sample in Test Seven Imaging 38

Figure 5.1a Changes in T_1 with SPIO Particle Size and Concentration 40

Figure 5.1b Changes in T_2 with SPIO Particle Size and Concentration 40

Figure 5.1c Changes in T_2* with SPIO Particle Size and Concentration 40

Figure 5.2 Comparison of 30nm SPIO particles Proton Relaxation Data 41

Figure 5.3 Explanation of transverse relaxation 42

Figure 5.4 Calculated Test Two T_2* Values 43

Figure 5.5 Consistency between Test Two and Three T2* values 44

Figure 5.6 Impact of Data Reduction Methodology 46

Figure 5.7 Predicted SPIO Optimal Concentration Range 48

Figure 5.8 Refitted Test One Sample Concentrations 49

Figure 5.9a BP Detection at .0000918nM SPIO Particle Optimal Concentration 50

Figure 5.9b BPM Detection at .0001836nM SPIO Particle Optimal Concentration 50

Figure 5.9c BPM Detection at .0002754nM SPIO Particle Optimal Concentration 50

Figure 5.10 Comparison of T_2 Changes between Top and Bottom of SPIO-BPM Samples 52

Figure 5.11 Bar Graph of Figure 5.9 53

List of Abbreviations

MNP	Magnetic Nanoparticle
SPIO	Superparamagnetic Iron Oxide
BPM	Biotinylated Polystyrene Microsphere
MRI	Magnetic Resonance Imaging
NMR	Nuclear Magnetic Resonance
IO	Iron Oxide
SEM	Scanning Electron Microscope
ROI	Region of Interest
RF	Radio frequency
T_1	Spin-Lattice Relaxation/Longitudinal Relaxation
T_2	Spin-Spin Relaxation/Transverse Relaxation
T_2*	Apparent transverse Relaxation Time/Magnetic Inhomogeneity Factor
FID	Free Induction Decay
TE	Echo Time
TR	Repetition Time
WB	Water Bath

CHAPTER 1

INTRODUCTION

1.1 Synopsis

Pathogen detection is a necessity in fighting human infection for food product industries and biodefense. Nuclear Magnetic Resonance (NMR) relaxation and Magnetic Resonance Imaging (MRI) have proven to be advantageous in comparison to other detection mechanisms to date such as quantitative Polymerase Chain Reaction (PCR) techniques, Raman spectroscopy [1, 2], fluorescence [1, 3], and colorimetry [1]. The development of new diagnostic platforms that utilize nuclear magnetic resonance (NMR) relaxation has garnered much attention due to their ability to measure bimolecular abundance with high sensitivity [4, 5], rapid disease detection [4, 6], and understanding of pathogen biology at the systems level [7]. It is necessary for these newly developed mechanisms to have high target specificity, almost instantaneous response time, repeatable identification, and capability to detect numerous varying target pathogens.

Nuclear magnetic resonance (NMR), is a phenomenon that occurs for nuclei possessing quantum spins that are subjected to a static magnetic field and then exposed to an additional second oscillating resonant magnetic field [8, 9]. The individual protons of the hydrogen atoms are the most commonly used particles in clinical applications that require this spin property [8]. Each proton will possess its own magnetic moment and will produce its own NMR signal when subjected to this phenomenon [8].

Nuclear magnetic resonance relaxation is the study of the interaction of electromagnetic radiation with matter when the specimen is exposed to a static magnetic field. A net magnetization is induced by the applied magnetic field. Normally, without the external magnetic field, the net magnetization is zero. The net magnetization is created by the sum of the spins such that each has their own precision-frequency. Quantum spins are found in protons, electrons and neutrons. Each unpaired electron, proton, and neutron possesses a spin of one half. In NMR, it is unpaired nuclear spins that are of importance.

For NMR of water, the spins of the hydrogen nuclei form a net magnetization aligned with an applied static magnetic field (B_0). At the resting state, the net magnetization vector of the protons is a combination of their spins aligned longitudinally (parallel to B_0) and having no net transverse magnetization components due to spins being out of phase. Figure 1.1a illustrates random spin orientations with no B_0 and 1.1b show how the quantum spins can either align with the field or in the opposing direction (anti-parallel). There are more spins aligned with the external magnetic field (low energy) than against it (high energy). As a result, the net magnetization has a longitudinal component aligned with the B_0 field while the transverse magnetization component is zero due to the spins rotations being in random phase.

Longitudinal = ∑nuclear spins

Transverse (rotation) = 0

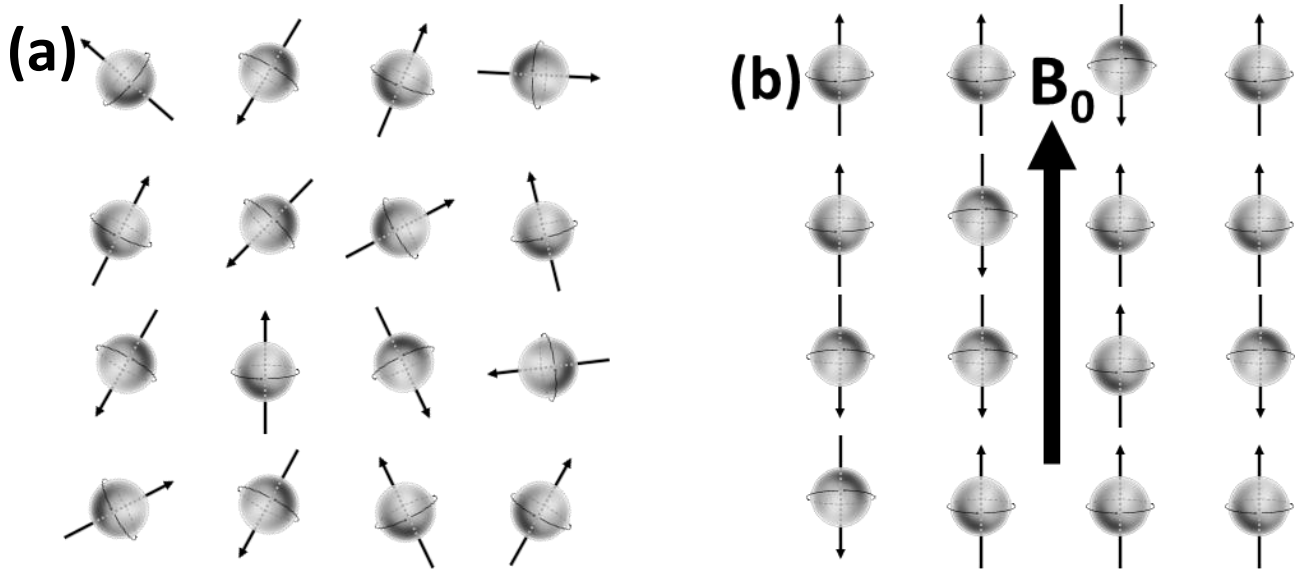

Figure 1.1 (a) Disordered water proton spins (b) Alignment of protons spins to magnetic field (B_0) direction

Hydrogen (in water) is chosen for clinical applications due to its abundance in biological tissues. While being controlled by the direction of the magnetic field, the protons will also precess about the axis of the field's direction. The precession frequency or the Larmor frequency of the protons is directly controlled by the applied field strength. More specifically, the precession frequency of each proton is directly controlled by its local magnetic environment and can be described by the Larmor equation found in Eq. 1 below [4].

$$\omega = \gamma B_{loc} \quad (1)$$

When placed in a magnetic field of strength B_{loc}, a particle with a net spin can absorb a photon of frequency ω. The frequency ω depends on the gyromagnetic ratio, γ of the particle [10]. Therefore each particle can only absorb a specific frequency depending on its γ. Their spins do not cancel each other out and a net spin is produced. The protons spin is its own property that gives it a magnetic moment or magnetic vector. When placed in a magnetic field, the protons magnetization vector will align itself with the external magnetic field.

To change the spin equilibrium of the protons, a Radio Frequency (RF) pulse is applied to the specimen. The applied RF pulse matches the precision frequency of some of the protons causing a change in the net magnetization vector and energy in the system. In a Magnetic Resonance Imaging (MRI) system, the RF pulse is tuned to the resonance frequency of the hydrogen proton. The application of the RF pulse to the water molecule's hydrogen proton causes it to align itself in the direction of the RF signal. The directional component of the specimen's magnetization is shifted from primarily longitudinal to only transverse. After the RF pulse is removed, the transverse magnetization of the protons decays and the longitudinal component recovers until the equilibrium position (static field direction) is reached.

The resonance frequency of the proton is the frequency at which the system is able to store and transfer energy with its greatest efficiency. To induce the shifting of directional magnetization components stated above, the electromagnetic RF pulse produced by an MRI must match the frequency of the resonance frequency of the hydrogen protons in order to induce the desired response for imaging. The electromagnetic energy is absorbed momentarily by the atomic nuclei causing a resultant change in spin equilibrium. Once the RF pulse is removed, the nuclei will regress from this new excited state back to its original equilibrium state over a period of time. This period of time is known as the relaxation time of the nuclei and is described as the time required for its transition between the transverse magnetization and longitudinal directions. The NMR signal collected by the MRI is formed by the electromagnetic energy released by the nuclei over its respective relaxation times.

The dynamic physical phenomenon of water protons spins transitioning back to their equilibrium positions is known as the relaxation of spins [8]. The system of spins relaxation to equilibrium is broken down into two components:

1. T_1 – recovery of longitudinal magnetization, aligned with the magnetic field
2. T_2 – decay of transverse magnetization, due to spins getting out of phase

Longitudinal relaxation (T_1) is also known as spin-lattice relaxation and is caused by longitudinal relaxation recovery. The difference in the number of spins in parallel and anti-parallel directions is what contributes to longitudinal magnetization. For T_1 relaxation, the proton spins relaxation causes a quantum emission of electromagnetic energy that is exchanged with the surrounding lattice. After RF pulse excitation, the precessing proton spins emit RF energy and revert back from a higher energy state to a lower state. The relaxation time constant T_1 can be calculated in Eq.2 by using the measured equilibrium magnetization (A_0) and longitudinal magnetization (A). The variables A and A_0 can also be referred to as the MR signal amplitude and MR signal amplitude at time (t) = 0 respectively. The time to diminish the difference between the longitudinal magnetization and the equilibrium magnetization is known as the spin-lattice relaxation time (T_1) [9]. As the static magnetic field strength is increased the values for T_1 also increase. Spin-lattice relaxation is performed by a 180° RF pulse using an inversion-recovery pulse sequence. As the spins rephase, the transverse magnetization grows as the longitudinal magnetization decays.

$$A = A_0 \times [1 - e^{-\frac{t}{T_1}}] \quad (2)$$

The second relaxation spin parameter that can be measured during NMR relaxation is the transverse relaxation (T_2). Transverse magnetization is caused by spins getting into phase coherence. The precession rate of the spins is altered by the interaction of their individual magnetic fields (spin-spin interaction). To find T_2 of a specimen a spin-echo procedure is commonly used that utilizes a 90° RF pulse. The transverse magnetization of the spins slowly decays during spin-spin relaxation causing a loss in phase. Spin-spin relaxation (T_2) can be calculated with Eq. 3. The T_2 relaxation rate is more strongly influenced by the local magnetic environment than T_1. For this

reason contrast agents are commonly used during MR imaging in order to change the local magnetic environment. By altering the magnetic environment the precessional frequency of the local nuclei is changed according to the Larmor equation. Although T_2 values are unrelated to the magnetic field strength, the stronger the field the more rapid the spins precession, thus changing the deviation in spin phases.

Typically T_1 tends to be longer than T_2. This can be seen by observing the width of the received NMR signal. The very quick spin-spin relaxation time creates very broad signals unlike T_1. The time limit of the signal or the signal line width in the transverse plane is represented by T_2. The line width measured for an NMR signal is used to find T_2 by measuring the line width at half-maximum. The line width at half maximum is equal to $1/T_2$. Although the originally measured line width can determine a T_2 value, the value is dependent on the inhomogeneity of the magnetic field. By using the experimental relaxation rate, a different form of T_2 known as T_2^* can be calculated (Eq. 4). Where T ‘ is the change in relaxation time due to magnetic field inhomogeneities.

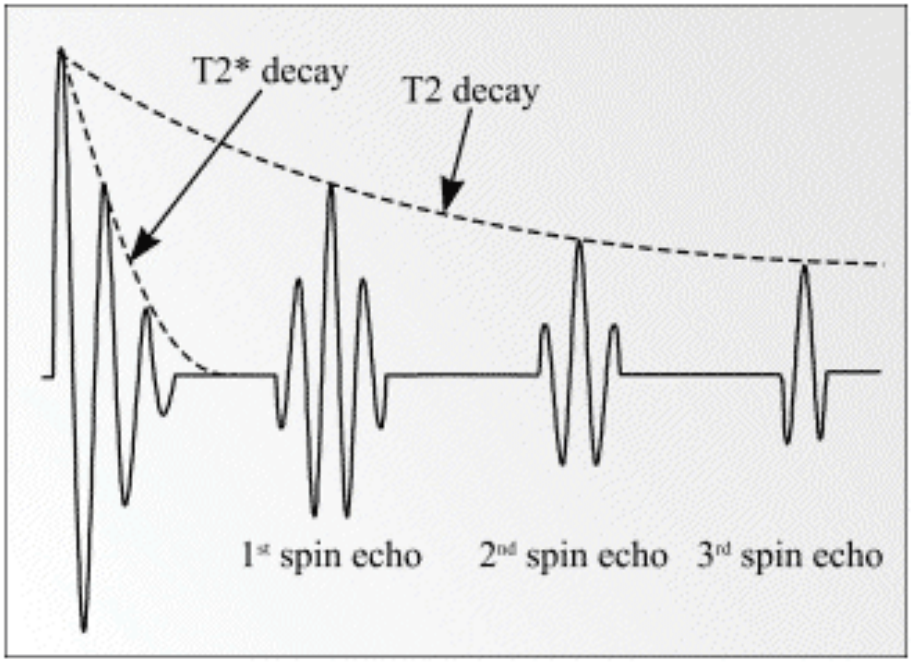

Figure 1.2 Schematic representation of T2 and T2* decay values derived from the MR signal collected. [25]

The inhomogeneity factor, T_2^* is more important for nuclei of higher precessional frequency. This can be explained by examining the Larmor equation. The resonance frequency for each nucleus is altered as the magnetic field varies through the specimen. Therefore, as the field varies, the frequency and the resultant NMR signal line

width also vary. To measure T_2*, a gradient-Echo sequence is typically used. The differences between a gradient echo from a spin –echo procedure is that the flip angle tends to be below 90° and the absence of a 180° RF rephrasing pulse. Without the presence of a magnetic gradient, the NMR signal produced is called Free Induction Decay (FID). T_2* is characteristic of the FID signal and will decrease exponentially as the FID signal decays. The relaxation time constant T_2* is found to be much faster than T_2 would predict. The differences between the two is that T_2* takes in to account the tissue specific spin-spin relaxation responsible for pure T_2 decay and is more sensitive to magnetic field inhomogeneity's. It is this second feature that tends to cause inconsistencies in the values for T_2*.

$$A = A_0 \times e^{-\frac{t}{T_2}} \tag{3}$$

$$\frac{1}{T_2^*} = \frac{1}{T_2} + \frac{1}{T'} \tag{4}$$

1.2 Thesis Structure

Chapter 2 reviews all subjects related to this thesis. First, it discusses the uses and characteristics of magnetic nanoparticles. The chapter provides an in depth look at the behavior of MNP's under an applied magnetic field and their influence on other particles. It describes how MNP's are used as a detection mechanism and their compatibility with varying environments. Finally, the chapter explains the similarities and differences between the different diagnostic platforms used for NMR relaxation.

Chapter 3 contains the experimental setup of this research. It provides the parameters used for all proton relaxivity data acquisition and SEM imaging. A short description of each parameter and its effects on the detection sensitivity, data reduction, and relaxation values is given. The technique utilized for the data reduction of each proton relaxation variable is also addressed.

Chapter 4 illustrates the procedure of each test performed during the course of the research. This chapter lists how and why each of the tests was conducted. It contains images of how the samples were positioned during

MR imaging; in addition to the values for each of the sample measurements. An explanation for the methodology of each procedure is also stated below in chapter 4.

Chapter 5 explains the results of each test performed by the MRI. The impact of the MNP core size on the proton relaxation data is described here, along with the necessary requirements for each relaxation variable to be used in pathogen detection. The reasoning for the selection of T_2 instead of T_2* as a viable parameter for target recognition is also discussed in this section. The data reduction of the research is further examined in order to compare the necessity for consistent data reduction methods and the reliability of the relaxation time values. The data collected from tests involving target detection provided an interesting discovery. The results of these tests were revealed to be of conflicting values than what was shown in previous reports. Finally, theories that were proposed for this unearthing were evaluated, thus finishing the chapter.

Chapter 6 concludes the research by providing a brief summary of the resultant understanding gained during this research. The final statement demonstrates that the detection resulted from the desired binding between the magnetic nanoparticles and the target molecules. The summary conveys the desired optimal MNP concentration for superior target sensitivity and its dependency on target molecule core size for the NMR detection mechanism.

An Appendix can be found at the end of the paper for all tables containing sample concentrations listed in Chapter 4.

CHAPTER 2

LITERATURE REVIEW

2.1 SPIO Nanoparticles

Nanoparticles have received increasing attention over the past few decades due to their unique characteristics, such as large surface-to-volume ratio and size-dependent optical and magnetic properties [4]. Their nontoxic nature along with their nanoscale dimensions hold much promise for further development in nanotechnology [11]. Nanoparticles provide specificity and multivalent affinity due to their ability to conjugate with specific ligands capable of attaching to their target molecules. This interaction allows for highly sensitive and selective diagnostic mechanisms for clinical use. It has been observed that these interactions can be detected by Raman spectroscopy, fluorescence, and colorimetric spectroscopy [4].

The relaxation value of water protons is greatly influenced by the local magnetic field surrounding the particles. SPIO nanoparticles have been reported to alter the magnetic resonance signal of surrounding water molecule protons by changing this local magnetic environment [4].The effective presence caused by magnetic particles on the relaxation time of water molecules operates at a significant distance from the particle [10]. “Evidence of this is found in the observation that MR images of livers containing the particles show reduced transverse relaxation time T_2 across the entire organ even though the phagocytic Kupffer cells containing the particles comprise only 2% of the mass of the liver” [10].

The enhancement of the relaxation time of water protons is due to the diffusion of water molecules between different magnetic environments created by the SPIO nanoparticles. This relationship between the spin-spin relaxation of hydrogen protons and the diffusion of the water molecules into areas of differing magnetic environments is represented by Eq. 5, where D, G, and τ are the spin diffusion constant, linear gradient, and the time between pulses respectively. The coherence of the phases of the precessing protons diminishes at a rate according to the local magnetic environment. As the water molecules diffuse into different areas, their alteration

in phases is controlled by the variation of the Larmor frequencies between each environment. These fluctuations in differing magnetic environments are the direct cause that modifies the resulting magnitude of the NMR signal received, hence to a varying T_2 [10].

$$\frac{1}{T_2} = \frac{D}{3}(\gamma \tau G)^2 \quad (5)$$

2.1a Comparison Between SPIO Nanoparticles Core Size

Research supports that different particle sizes can have a contrasting effect when influencing the local magnetic environment of surrounding water molecules. Contemporary research focuses on the use of nanoparticles by replacing the previously used micron sized particles. Unlike nanoparticles, microparticles have lower efficiency and poorer binding ability due to their comparatively lower surface to volume ratio [12].

Nanoscale dimensions offer a wide array of advantages over micron size particles. First, microbeads typically take longer to interact with the target molecules in suspension [12]. Second, micron size particles have proven not to be completely stable in suspension and can cause unwanted precipitation leading to inefficient separation and detection [12, 11]. Third, by reducing the particle dimensions and increasing the surface to volume ratio, the available adsorptive areas increase drastically (Figure 2.1) [12, 13]. Fourth, nanoparticle's smaller size allows for easier diffusion to areas of denser target molecule concentration thereby increasing their interaction [12]. Finally, under an applied magnetic field, larger particles tend to aggregate causing loss in signal detection [4, 14].

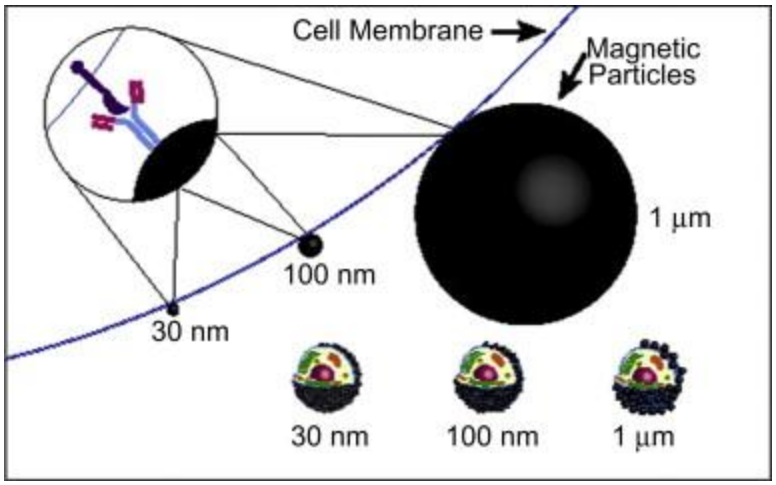

Figure 2.1 Diagram comparing the availability of differing particle sizes to be attached to an immunomagnetically labeled cell. The particles with a smaller sized diameter are more capable of attaching on the cell surface than larger (micron) sized particles because of less steric exclusion. [12]

2.1b SPIO Nanoparticle Stability and Compatibility

The most problematic issue regarding nanomaterials used for biological applications is their compatibly with different biological environments. Research has shown it is imperative to design these materials against extreme conditions to prevent potential signal loss [12]. Without proper magnetic nanoparticles (MNP) preparation, the nanoparticles can potentially oxidize, hence causing the formation of antiferromagnetic oxides resulting in a significant loss in magnetic moment [15]. Increasing concern for the synthesis of air-stable nanoparticles with high saturation magnetization capable of withstanding extreme conditions has thus developed for the optimization of contrast agents [15, 16].

Efforts have been made to prevent any loss in magnetic moment by improving the coating layer surrounding the nanoparticle metal core [15, 16]. Examples of these preventive measures consist of inserting the metallic particles into polymer matrixes or passivating them with an oxide shell, gold, or carbon [15].

Iron oxide nanocrystals are commonly coated with hydrophobic surface ligands such as oleic acid [11]. The hydrophobic oleic acid layer provides surface iron lattices analogous to bulk structures and strong binding of the layer to the iron sites [11]. As a MRI contrast agent, the layer protects the particle surface from water proton interaction, causing a decrease in the average proton relaxivity [11]. The hydrophilic polymer coatings help prevent magnetic field assisted particle/particle aggregation of MNPs [14]. The measurable proton relaxation rates are

reliant on hydrophilic characteristic of the coating layer [11]. Figure 2.2 illustrates that the iron oxide nanoparticles coated with PEI exhibit the highest proton relaxivity R_2. Proton relaxation rate (R_2) is the reciprocal value of the spin-spin relaxation time variable T_2. Nanoparticles coated with the oleic acid proved to have a much smaller R_2 value than that of the PEI coating [11].

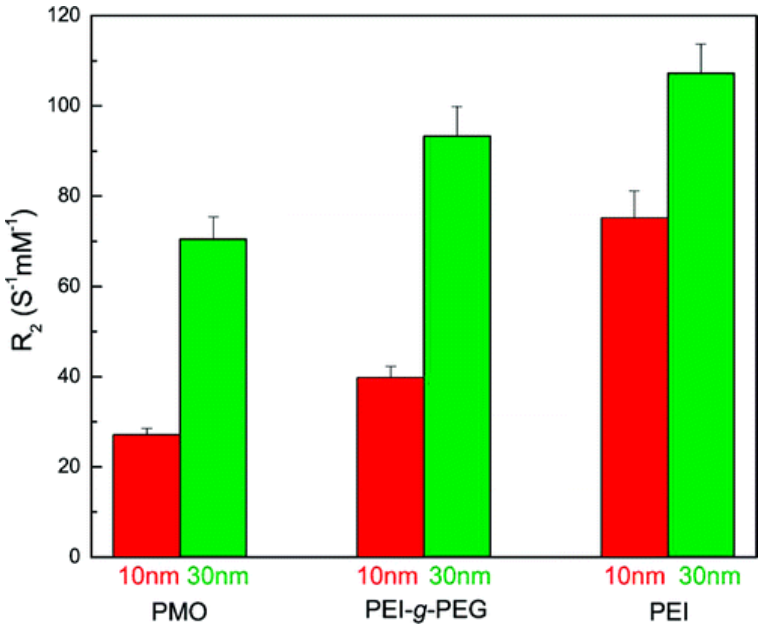

Figure 2.2 Dependency of the proton relaxation rate on the iron oxide contrast agent's coating layer hydrophilicity and particle size. [11]

Different coatings on MNPs can alter the hydrodynamic size of the particle. For example, an iron oxide (IO) particle with a 30 nm core was found to have a hydrodynamic size of 56.6nm when coated with PEG-g-PEI, but smaller hydrodynamic sizes of 44-45 nm when coated with PEI or PMO [11]. Furthermore, it was reported that proton relaxivity is greatly influenced by the size of the particles. Smaller particles with a core size of 10 nm were shown to have smaller relaxation rates than larger 30nm core size particles. Even with different particle coatings these results remained consistent. It was suggested that the results were due to differences in surface spin anisotropy, which tends to be more effective for smaller core size particles because of their larger surface area to volume ratios [11].

Table 2.1 Proton Relaxivity Data comparing its impact on SPIO Nanocrystal Core Size and Polymer Coating [11]

		PMO coated nanoparticles		PEG-g-PEI coated nanoparticles		PEI coated nanoparticles	
relaxivity ($s^{-1}mM^{-1}$)	**Deionized H_2O**	**10 nm**	**30 nm**	**10 nm**	**30 nm**	**10 nm**	**30 nm**
r_1	0.01	7.8	10.9	11.2	14.1	21.5	29.0
r_2	0.54	27.2	70.5	39.8	93.3	75.2	107.3
r_2^*	0.51	28.2	72.2	34.1	87.5	71.3	98.7

r_1 = longitudinal relaxation rate; r_2 = traverse relaxation rate; and r_2* = effective traverse relaxation rate.

As shown in Table 2.1, Magnetic nanoparticles influence on proton relaxivity appear to be highly dependent on their surface coating, particle size, and the hydrophilicity of inner capping ligands. These three factors are imperative when selecting nanoparticles for diagnostic platforms involving biological media. The SPIO particles in this study where chosen to have nanoscale dimensions and a protective polymer coating to prevent oxidation and increase detection sensitivity.

2.2 Detection Mechanism

NMR detection is based on aggregate formation (Figure 2.3) or dissociation (Figure 2.4) when MNPs bind to the desired target molecules [4]. The streptavidin coated SPIO nanoparticles readily bind with the target biotinylated polystyrene microspheres (BPM). The biotin-streptavidin conjugation was used in this study to mimic the binding interactions that would occur between an antibody and an antigen. The spin-spin relaxation time (T_2) is altered due to the formation of these clusters which cause the dephasing rate of nearby proton spins to increase [4]. The precessional frequency of a protons spin is strongly controlled by the local magnetic environment surrounding the water molecule's hydrogen proton according to the Lamor equation [4]. SPIO nanoparticles will cause changes in the local magnetic fields homogeneity thereby altering the dephasing of nearby water protons. The SPIO nanoparticles can enhance the return of the water protons magnetization directional components from

the excited state back to the equilibrium state (static field direction), thus shortening their relaxation time values [4]. The aggregation of SPIO nanoparticles by SPIO-BPM interactions produces stronger local magnetic fields due to the coupling of SPIO nanoparticles magnetic moments. This alteration of the local magnetic environment is the basis of NMR detection. The mechanism aims at determining the presence of the specific targets by measuring changes in spin-spin relaxation (T_2) after the formation or dispersion of the SPIO-BPM aggregates [4, 6, 14, 17].

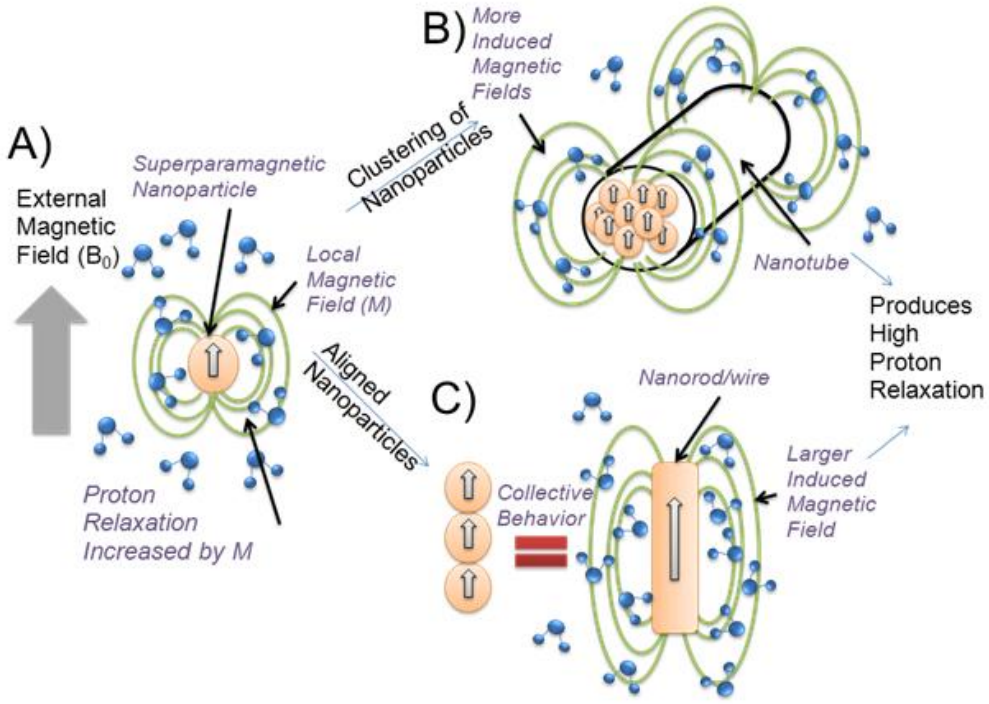

Figure 2.3 Illustration describing the effects of superparamagnetic contrast agents on surrounding water molecule protons. (A) The alignment of the MNP's magnetic moment to the direction of the applied field, which creates local magnetic fields causing an increase in spin-spin relaxation of the local protons. (B) Formation of nanoparticle clusters creates larger local magnetic field inhomogeneities thereby further increasing T_2 relaxation of nearby protons. (C) Nanoparticles are aligned in a linear array along a nanowire. The clustering of the nanoparticles in this format further improves the coupling of the nanoparticles magnetic moments thus improving proton relaxation. [18]

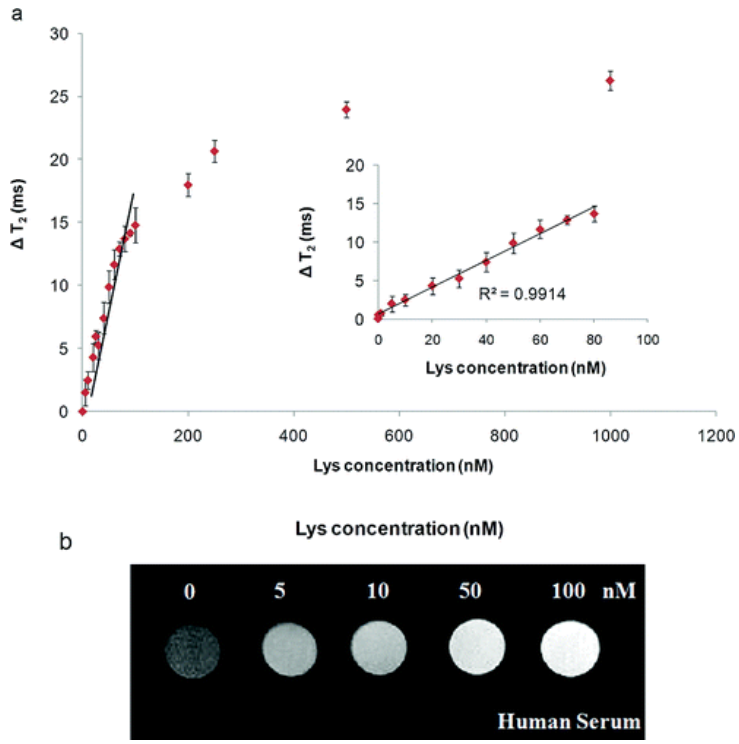

Figure 2.4 The disassembly of MNP-Lys aptamer clusters after the addition of the lysozyme protein. Detection was proven from the resulting increase in T_2 relaxation time with increasing lysozyme concentration additions. (a) Determination of the lysozyme detection range. (b) T_2 weighted MR images of increasing lysozyme concentration. [4]

The utilization of these NMR techniques allows for electronic data acquisition instead of previously used bulky optical components. The signal detection is much faster than with surface structure-based devices because of their ability to detect in the specified area instead of relying on the diffusion of the targets to the sensing elements [4, 5, 6]. This technology has the potential for easier, quicker, and higher-throughput sensing operations than its predecessors. Assays that employ these NMR techniques for signal detection measurements also have the capability to be executed in turbid samples with few or no preparation steps [5, 17].

A consequence of this mechanism is the precipitation of the molecules after the formation of the SPIO-BPM clusters. The settling of the SPIO-BPM clusters could reduce the average number of water hydrogen protons that could diffuse between the SPIO nanoparticles magnetic domains. Thus the precipitation of the SPIO-BPM clusters could potentially alter the acquired relaxation values thereby reducing the validity of the BPM detection. By combining the SPIO nanoparticle sensor with lower concentrations of the target molecule (BPM), the precipitation of the clusters can be avoided [4, 19]. Although this method was shown to prevent signal loss due to

unwanted settling, the measurements performed were limited to only target molecules of very low molecular weights.

Another problem to avoid in SPIO nanosensors is the assembly or disassembly of SPIO clusters due to random binding sequences other than that of the target sequence (streptavidin-biotin) [4, 17, 19]. SPIO nanoparticles are capable of binding with various ligands that have specific binding characteristics to provide specificity and multivalent affinity [4, 5, 17, 20]. The selectivity of the magnetic nanosensors is an imperative parameter to be considered. The example shown in Figure 2.5, displays previous research that has proven that these complications (non-specific binding) can be reduced by improving the selectivity of the target molecules which can provide only slight alterations in T_2 [4]. The interference with detection of the target molecules (BPM) in biological media is highly dependent on the selectivity of the SPIO nanoparticles.

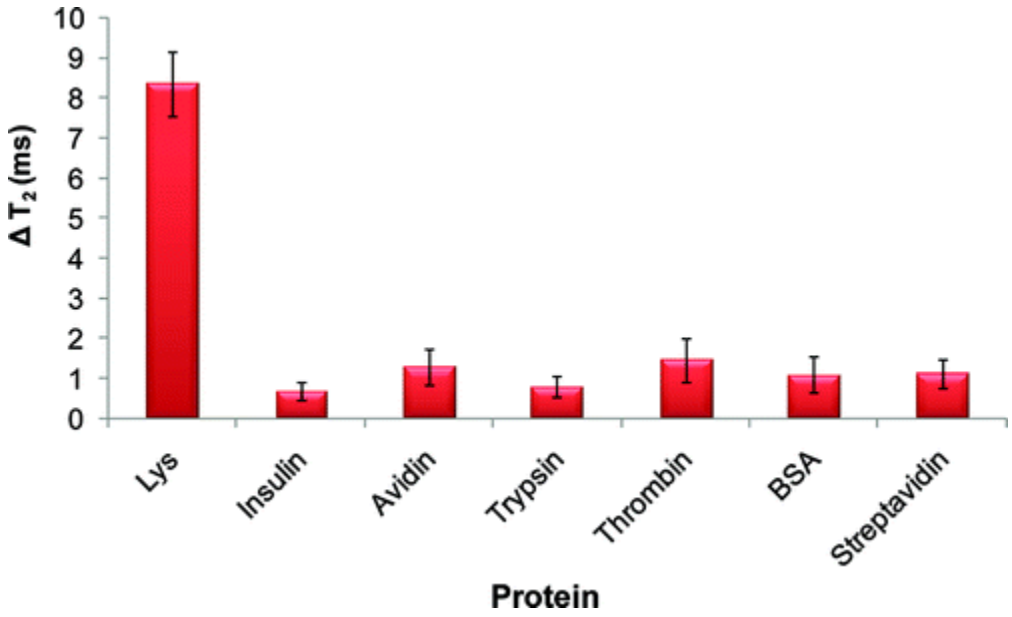

Figure 2.5 The change of T_2 after the addition of the lysozyme target molecule. The chart was to prove the selectivity of the magnetic nanosensors from binding from other undesired interactions that could interfere with the lysozyme detection. [4]

SPIO nanoparticles have shown to remain highly stable even when exposed to large temperature fluctuations and different ionic media [5, 6, 21]. Small differences in target conjugations could be detected by T_2 measurements within a multitude of different buffer conditions. Research has demonstrated that diagnostic

platforms utilizing NMR relaxation techniques are capable of performing selective measurements reliably and at various temperatures without the interference of T_2 measurements from target mismatches [5, 6].

The SPIO nanosensor can detect the target BPM in solution by measuring the changes in spin-spin relaxation (T_2) upon SPIO-BPM conjugation. The interaction of the SPIO-BPM molecules will create larger clusters that can modify the original (SPIO nanoparticles only) T_2 values. It is vital that the resultant T_2 changes occur primarily from specific binding (streptavidin-biotin) between the SPIO nanoparticles and the target pathogen (BPM) rather than by nonspecific effects.

2.3 Differences between NMR Diagnostic Platforms

NMR relaxometer design has the potential to increase detection sensitivity, lower sample volume, provide multiplexity, and increase signal-to-noise. To date, Benchtop NMR and clinical systems have been the most researched as NMR detection assays [4, 5].

Clinical systems such as MRI's allow for parallel measurements at higher throughput with a minimum sample volume of 50µl [6, 22]. The average cost of running an MRI test usually costs around $500 per hour. The sensitivity and throughput of an MRI assay can be enhanced through increasing the number of well plates or by decreasing the total sample volume [4]. An increase in the number of well plates has the potential to improve the quantity, quality, and swiftness of data collected [4]. Typically MRI's have a magnetic field strength of 1.5 to 3.0 Tesla, but there are more powerful MRIs available with field strengths exceeding 11.4 Tesla. At their lowest strength of 1.5 Tesla, SPIO nanoparticles are almost entirely saturated and create the desired, local magnetic inhomogeneities [13].

Figure 2.6 Image of a closed (traditional) MRI scanner [23]

Benchtop relaxometers can have magnetic field ranges from .17 to 1.41 Tesla with frequency ranges from 7.5-60 MHz. The proton NMR frequency and magnetic field strength influence both the detection sensitivity and the overall testing time. Another benefit found with most benchtop relaxometers is their capability of controlling the sample temperatures during testing. Heating elements with temperature sensors can be used for better temperature control [5]. These heating elements can also be added to the microfluidic systems of chip sized NMR sensors [5].

By miniaturizing an entire NMR system even further, the mechanism could potentially perform measurements on even smaller sample volumes and in a multiplexed fashion [5, 17]. Miniaturized systems fitted with microfluidics allow for easier control and manipulation of small volumes of liquid. In addition to this, it can reduce the signal to noise ratio, lessen the need for spatial homogeneity of the magnetic field. Finally, it offers additional magnetic separation of target molecule concentrations from a parent specimen [5]. Multiple planar microcoils are typically arranged in an array to perform multichanneled detection instead of the common field gradient coil design [5]. This design allows for easier device miniaturization and portability. Miniaturized sensors are designed to be self-contained and portable devices and have many other potential methods for further size reduction [17].

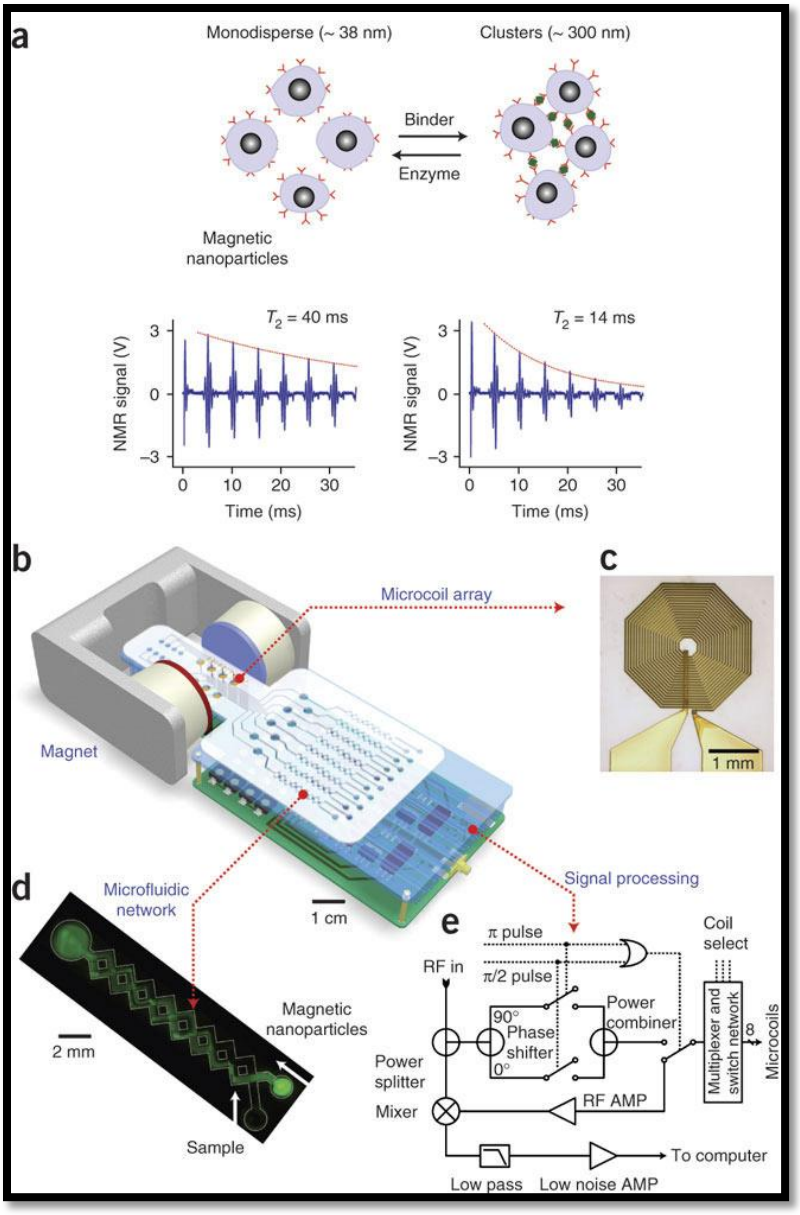

Figure 2.7 (a) The binding of MNP's to their targets forming clusters. The formation of these clusters induces larger magnetic inhomogeneities, thereby increasing the dephasing rate of the nearby water proton spins and reducing the spin-spin relaxation time (T_2). (b) A NMR systems schematic diagram. (c) An image of a microcoil used for the NMR system. (d) An image of a microfluidic network. (e) Diagram of the NMR electronics used in the NMR system to perform T_1 and T_2 measurements. [5]

In one report researchers developed a chip-NMR biosensor capable of perform eight-multiplexed measurements in 5-10µl sample volumes [5]. A schematic of the chip-NMR system and its microfluidic system is shown above in Figure 2.7c and Figure 2.7e. The NMR system was fitted with microfluidic networks that provided chaotic advection through the meandering channels, allowing for easier manipulation of MNP and target molecule mixing. The chip-NMR biosensor permitted more homogeneous radio-frequency magnetic fields with less electrical

resistance. It could also detect multiple targets in mass-limited samples and reduced the usage of expensive reagents.

The chip-based DMR (diagnostic magnetic resonance) system was reported to have a sensitivity of as low as 1 x 10^{-12}M. It was capable of performing sensitive detection and multiplexed identification of different target molecules. Their design was compared to a benchtop system with a similar magnetic field strength. Both systems measured the T_1 and T_2 relaxivities of water containing MNPs bound with their target molecules using inversion-recovery pulse and CPMG sequences respectively. The results of both tests showed excellent agreement (Figure 2.8).

Standard benchtop NMR systems require sample volumes greater than 300µl and can only process one sample at a time [5]. Unlike the benchtop system, the chip-NMR sensor from the design above can have a sample volume as low as 5µl per coil. Multiplexed measurements can be performed by each coil independently and is theoretically only limited by the number of coils fitted on each chip [17]. Chip-NMR sensor's permanent magnets are portable and are capable of producing polarizing magnetic fields, B_o =0.1 -0.5T. The chip-NMR system greatly outperformed the benchtop relaxometer mass sensitivity. It achieved a minimum detection of 1.0ng of avidin in a 5µl sample. The improved mass sensitivity can be attributed to the device miniaturization of the microcoil, which enabled stronger radio frequency field generation with increased filling factors in small sample volumes [5, 17].

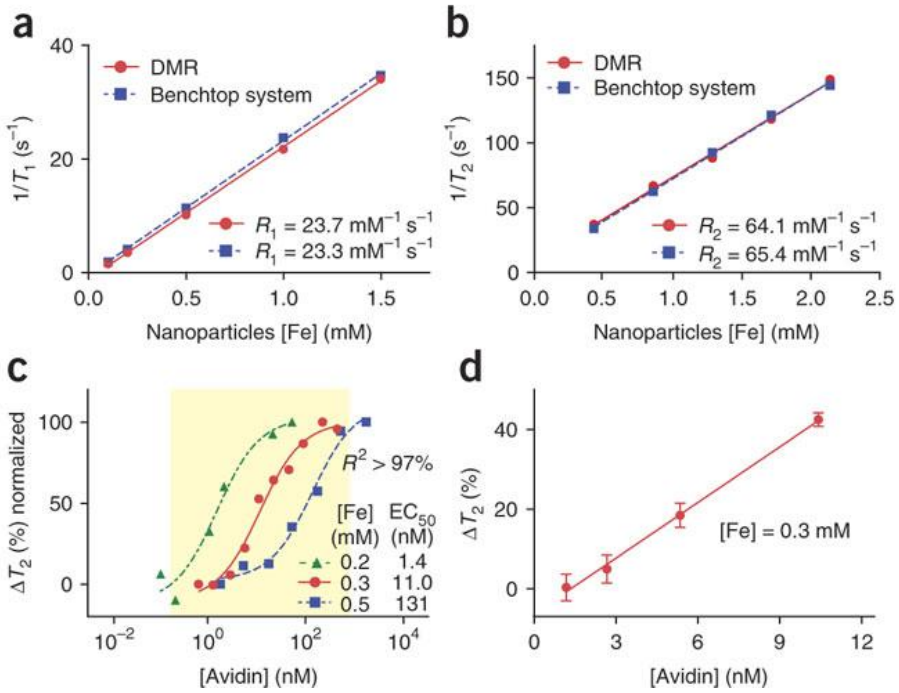

Figure 2.8 (a,b) Graphs indicate a comparison between a commercial benchtop relaxometers and the newly developed DMR systems measurements of T_1 (a) and T_2 (b). (c) The resultant change in T_2 with increasing additions of avidin concentration to biotinylated mangetic nanoparticles. (d) A closer inspection of the minimum mass-sensitivity capable by the DMR system for detection of the target molecule. [5]

Miniaturizing the source of the external magnetic field produces complications. One problem is a low NMR signal level intensity is collected due to the small sample volume and low magnetic field strength [5]. Microfluidic systems onto chip-NMR systems have shown to overcome these obstacles. Low signal-to-noise ratio has commonly been attributed to the design of the planar coils because of their high series resistance [24]. NMR probes consisting of electroplated planar microcoils integrated on a glass substrate with etched microfluidic channels are a common design for chip sized relaxometers. Reducing the diameter of the microcoils has indicated potential to improve the mass-sensitivity of the spectrometer [24].

An example of an actual microcoil used for NMR detection can be found in the image above in Figure 2.7c. Radio frequency magnetic fields are produced by the microcoil in order to induce and an excitation of the samples and receive their resulting NMR signal. The material selected for the metal lines electroplated on the microcoil is imperative for minimizing the electrical resistance and hence thermal noise of the microcoil [5]. The reduction of the thermal noise is vital for preventing its interference with the NMR signal collected by the microcoil.

Currently, the largest obstacle inhibiting sensitivity is designing the spectrometer to prevent probe-induced static magnetic field distortions. By minimizing the size of NMR detection coils, the mass-sensitivity has proven to increase drastically for mass-limited samples [24]. The majority of micro-scale NMR diagnostic platforms focus on solenoid-type microcoils wound around a capillary. To improve this design the planar microcoils can be built using processes based on photolithography techniques [24]. The utilization of micromachined coils has numerous advantages, such as the ability to fabricate micron sized planar coils and the availability of chip-based microfluidic system integration. Further developments in microfabrication can lead to possible improvements for NMR spectrometer design by enhancing sensitivity, lowering cost, and increased portability.

CHAPTER 3

EXPERIMENTAL SETUP

The relaxation times of each the samples were measured using a human knee Xmit/Rcv RF coil in a clinical Siemens Verio 3 Tesla MRI Scanner. Proton density, Repetition time (TR) and Echo Time (TE) are some of the conditions and sequence parameters that affect the overall acquisition time and the imaging contrast. The Echo Time (TE) is the time between the application of the RF excitation pulse and MR echo signal collection. The MR echo signal is collected at time TE after excitation. The time between RF excitation pulses is the repetition time (TR).The repetition times were selected in order to guarantee the recovery of the transverse magnetization back to the longitudinal equilibrium condition. A long TR time allowed for maximum signal available for the next TR. This gave less T_1 weighting, and more T_2 and proton density weighting. The tradeoff for improving the results due to a long TR, is the lengthening of the overall scan time. The sequences performed applied a constant TR and varied the time of inversion (TI) for T_1 scans or TE for T_2 and T_2* scans listed below under each variables sub-section.

3.1 T1 Inversion Recovery (T_1) Parameters:

The sequence type chosen for T_1 measurements for all MR testing was a non-selective adiabatic inversion with slice-selective spoiled gradient-echo acquisition. A standard coronal slice of approximately 5mm was used to create the slice images of each of the samples. Each sample image was fitted within a 128 x 128 pixel matrix to encompass the entire sample area. A total of 54 time of inversion (TI) echo times ranging from 5.6 to 3000 ms were used for each sample with a TR time of 5 seconds between each RF inversion pulse. The total acquisition time was 10.6 hours for the entire procedure. The readout flip angle was performed at 60 degrees and a readout bandwidth of 289 Hz/Pix. The inversion times (TI) used for T_1 imaging can be found in Table3.1 below.

Table 3.1 Inversion Times (TI) used for imaging of T_1 (ms)

5.6	10.0	20.0	30.0	40.0
50.0	60.0	70.0	80.0	90.0
100.0	110.0	120.0	130.0	140.0
150.0	160.0	170.0	180.0	190.0
200.0	220.0	240.0	260.0	280.0
300.0	320.0	340.0	360.0	380.0
400.0	425.0	450.0	475.0	500.0
550.0	600.0	650.0	700.0	750.0
800.0	850.0	900.0	950.0	1000.0
1200.0	1400.0	1600.0	1800.0	2000.0
2250.0	2500.0	2750.0	3000.0	

3.2 Transverse Relaxation (T_2) Parameters:

To calculate the T_2 values of each sample a slice-selective spin-echo MRI sequence type was employed. Similar to the T_1 measurements, a 5 mm coronal slice with an image matrix size of 128 x 128 pixels was used to create each sample image. The acquisition time of the entire procedure was roughly 9.25 hours for the 52 spin-echo times (TE) collected and a TR time of 5 seconds between each RF excitation pulse. The excitation flip angle was 90 degrees, refocus pulse was 180 degrees, and a readout bandwidth of 355 Hz/Pix. The echo times (TE) used for T_2 imaging can be found in Table 3.2 below.

Table 3.2 Echo Times (TE) used for imaging of T_2 (ms)

7.0	7.5	8.0	8.5	9.0
9.5	10.0	11.0	12.0	13.0
14.0	16.0	18.0	20.0	25.0
30.0	35.0	40.0	45.0	50.0
60.0	70.0	80.0	90.0	100.0
125.0	150.0	175.0	200.0	225.0
250.0	275.0	300.0	350.0	400.0
450.0	500.0	550.0	600.0	650.0
700.0	750.0	800.0	850.0	900.0
950.0	1000.0	1100.0	1200.0	1300.0
1400.0	1500.0			

3.3 Magnetic Inhomogeneity Factor (T_2*) Parameters:

A slice-selective spoiled gradient-echo MRI sequence type was chosen for all T_2* measurements. Each image slice was 4 mm thick and created an image matrix size of 128 x 128 pixels. More echo times (TE) were used for T_2* measurements than that of T_1 and T_2 to ensure sufficient data collection. The procedure was completed

within 4.25 hours to cover the 61 TE chosen and a TR time of 1.0 sec between each RF excitation pulse. The excitation flip angle was 90 degrees and a readout bandwidth of 488 Hz/Pix. The TE used for T_2* imaging can be found in Table 3.3 below.

Table 3.3 Echo Times (TE) used for imaging of T_2* (ms)

3.0	3.5	4.0	4.5	5.0
5.5	6.0	6.5	7.0	7.5
8.0	8.5	9.0	9.5	10.0
11.0	12.0	13.0	14.0	15.0
16.0	17.0	18.0	19.0	20.0
22.0	24.0	26.0	28.0	30.0
32.0	34.0	36.0	38.0	40.0
45.0	50.0	55.0	60.0	65.0
70.0	75.0	80.0	85.0	90.0
95.0	100.0	110.0	120.0	130.0
140.0	150.0	160.0	170.0	180.0
190.0	200.0	225.0	250.0	275.0
300.0				

3.4 Data Reduction

Data reduction of the acquired MRI signal intensities was performed for every test procedure and relaxation time. The T_2 and T_2* values were calculated by plotting the MRI signal intensities versus echo times according to Eq. 3 and 4 respectively. A decay curve was fitted for each samples data series plot. The resultant equation from the fitted trend line was used to extrapolate the values for T_2 and T_2*. A nonlinear curve fitting method based on Eq.2 was used to determine the magnitude of the MRI signals at different inversion time points, and to calculate the T_1 relaxation time of each sample.

3.5 SEM

SEM images were taken by a JEOL JSM 7000F SEM instrument. The samples were deposited onto a copper 400 mesh grid followed by drying. Afterwards, the samples imaged under a magnification of 70,000-X at an accelerating voltage of 20 kV. No sputter coating was required since the particles were already conductive.

CHAPTER 4

TEST PROCEDURES

Table 4.1 Test Procedures

Test Number	MRI Scanning Procedures
Test One	MRI scan of different SPIO nanoparticle core sizes and relaxation rates
Test Two	MRI scan to determine T_2* dependence on SPIO nanoparticle concentration
Test Three	MRI scan to test the validity and reliability of T_2 and T_2*
Test Four	MRI scan to detect polystyrene microspheres (BPM) using T_2
Test Five	MRI scan to verify the optimal concentration
Test Six	MRI scan to confirm the T_2 values and the trend to increase with BPM concentration
Test Seven	MRI scan to validate particle settling during imaging using T_2

4.1 Test One: Relaxation Time Dependence on SPIO Nanoparticle Concentration

Test One samples included 38 samples, 4 of which were pure water samples, 16 included only the 10nm MNP, and the remaining 18 contained only the 30nm MNP. The magnetic nanoparticles were superparamagnetic iron oxide (SPIO) nanoparticles with an amphiphilic polymer coating conjugated with streptavidin. These were acquired from the company Oceannanotech. SPIO nanoparticles tested were of two different inorganic core sizes, 10nm and 30nm. Each nanoparticles hydrodynamic sizes was about 8-10nm larger than its inorganic core size. All samples used were sonicated prior to MRI testing.

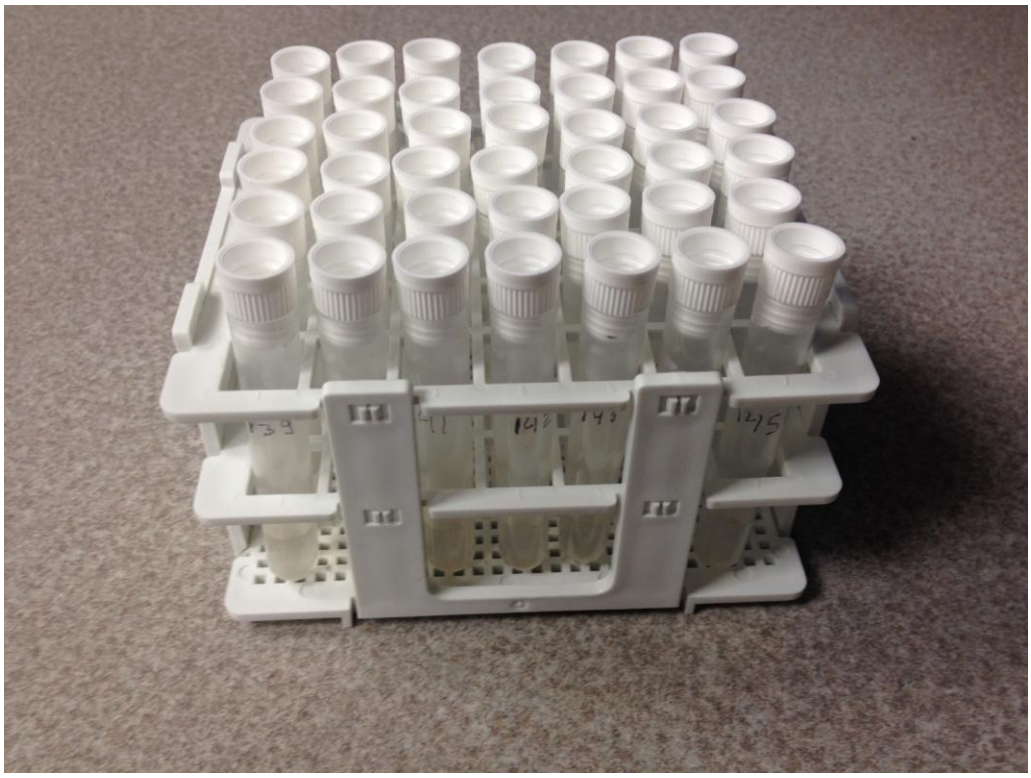

Figure 4.1 Image of the test tube rack and test tube samples used for Tests One through Seven.

The first test was aimed at determining the changes of the T_1, T_2, and T_2* relaxation times with increasing concentrations of the SPIO nanoparticles. Measured concentrations of the SPIO nanoparticles were first dispersed into test tubes containing deionized water. Each test tube sample for all tests contained 1ml of deionized water. The samples containing the SPIO nanoparticles increased over a range of 18 SPIO nanoparticle concentrations from low to highly concentrated. The range of SPIO nanoparticle concentration for the 10nm and the 30nm were of similar molar values (Figure 4.2).

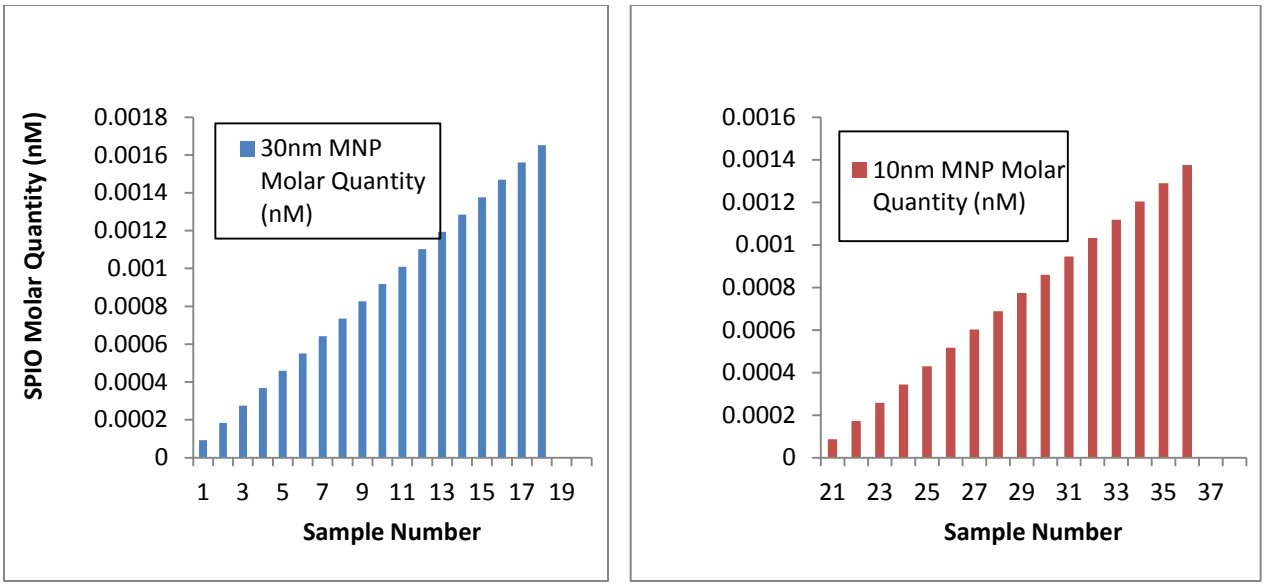

Figure 4.2 Test One sample's SPIO nanoparticles molar quantities

Two different testing procedures were used in the experiment. These procedures measured the respective T_1, T_2, and T_2* relaxation values of each of the SPIO nanoparticles. Multiple properties of the SPIO nanoparticles were calculated and measured in test one. The first property tested measured the differences between the particle sizes and their individual relaxation values. The second targeted advantages and disadvantages between T_1, T_2, and T_2*. It was necessary to compare their accuracy, consistency, and scan rate of each of the relaxation times in order to determine the most optimal variable for use as a detection mechanism. The final component of Test One was to calculate the contour of the curve for each relaxation variable versus particle concentration.

The 38 samples were held in a test tube rack and were tested simultaneously under 3.0 Tesla MRI for their T_1, T_2, and T_2* values. The test tube rack and samples were initially submersed in a water bath to create a more consistent magnetic medium, potentially increasing the accuracy of the results due to improved signal homogeneity. The tests were repeated without the water bath for comparison of the results and to determine the potential impact of the medium. The background image of the water bath was also calculated for reference to the sample data for all of the proceeding tests.

To prove the predicted SPIO nanoparticle concentration and particle size, 4 of the MNP samples from Test One were imaged under a Scanning Electron Microscope. The images were magnified to 70,000X. A slight measurable offset for the expected SPIO nanoparticle concentrations of Test One samples had occurred due to the imprecision of the original pipette used. The SPIO nanoparticle concentration was calculated from the SEM images and the concentrations were re-fitted according to their expected relaxation values. The re-fitted concentrations were used for later comparisons to the T_2 results found in Test Three.

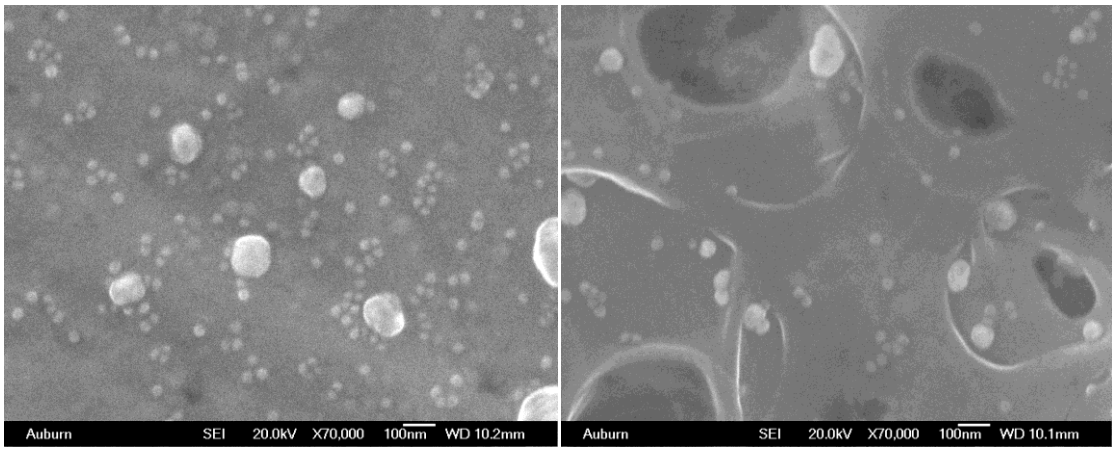

Figure 4.3 SEM images of the 30 nm SPIO nanoparticles used in Test One.

4.2 Test Two: T_2* Minimum SPIO Nanoparticle Concentration Detection

Test Two included a total of 30 samples. Of these, only two were pure water samples. Based upon information gathered from Test One, it was decided that further testing would only include the 30nm inorganic core size SPIO nanoparticles. Also, T_2* was predicted to be the most applicable parameter from Test One and was therefore chosen as the only relaxation variable used for this test.

A gradient echo procedure was used to measure T_2* in Test Two. Test Two focused on determining the curve contour for a lower concentration range of SPIO nanoparticles for T_2*. To obtain the lower concentration range, samples 17 and 18 from Test One were diluted to form the 28 new samples used in Test Two (Figure 4.4). Of the 28 samples containing SPIO nanoparticles, 2 of them contained the same SPIO nanoparticle concentration as samples 1 and 2 from Test One. This was to assess the reliability and validity of the results between Test One and Two. The purpose of Test Two was to find the optimal concentration values to be used as a detection mechanism and to predict the expected T_2* values over a wide range of SPIO nanoparticle concentrations.

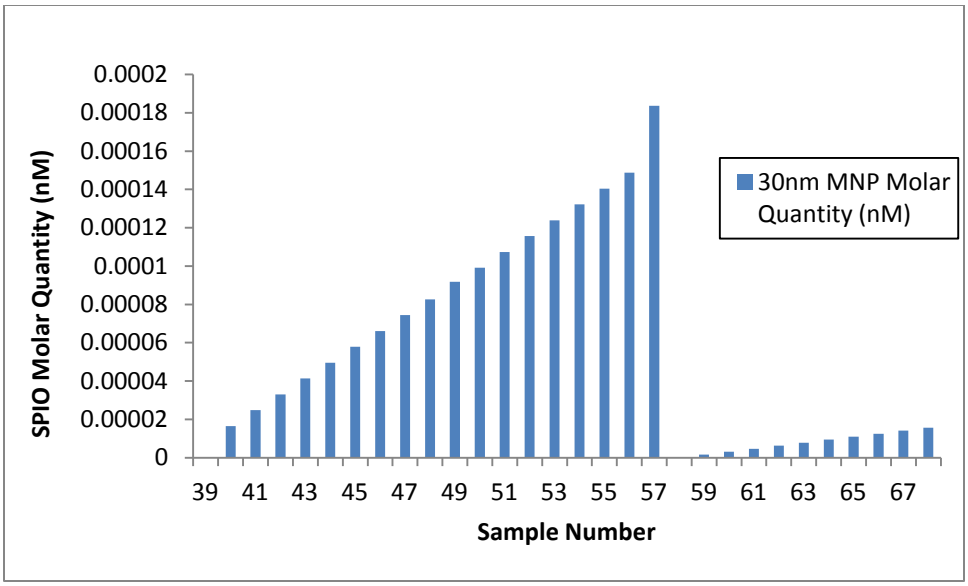

Figure 4.4 Test Two sample's magnetic nanoparticles molar quantities

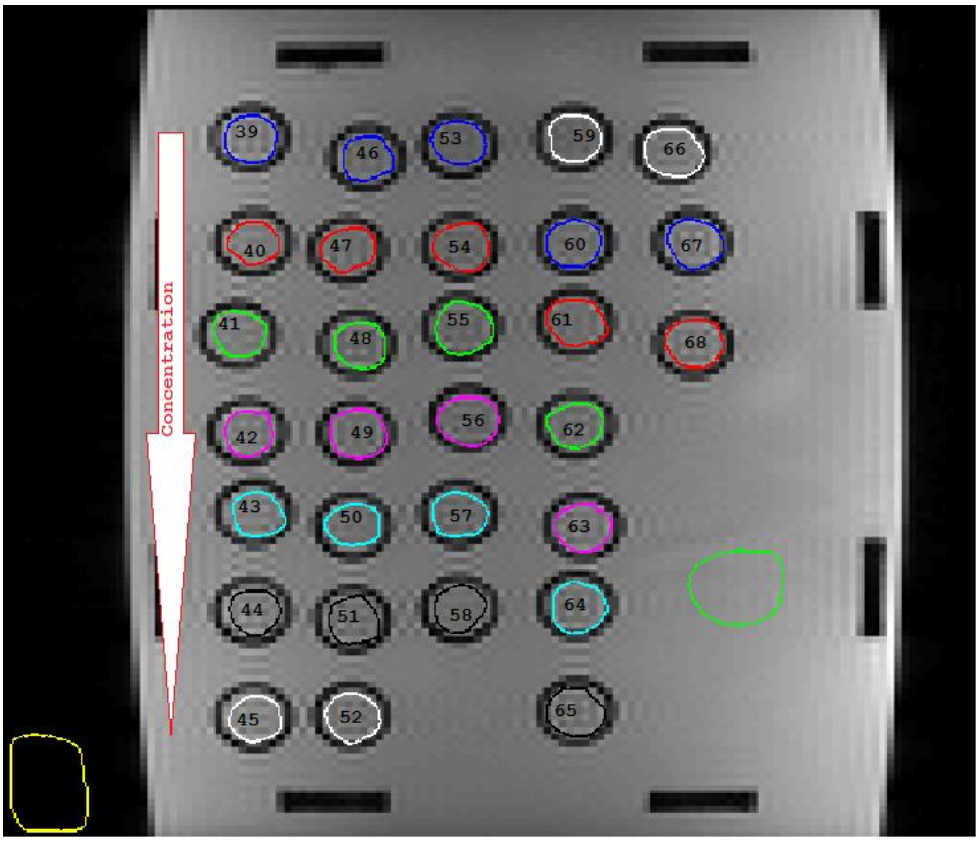

Figure 4.5 MR image of the regions targeted for each sample. The numbers listed are the respective samples numbers from Test Two. The arrow indicates that the concentration of SPIO nanoparticles decreases down each row. Areas circled outside of the test tubes (green and yellow) were measured for their relaxation values in order to be used as a referecne.

4.3 Test Three: Validity and Reliability of T_2 and T_2*

Only the 30nm inorganic particle size was selected for use in all proceeding tests due to the information collected from Test One and Two. Based on results from Test Two, T_2* was not considered a reliable predictor of concentration values due to lack of consistent findings between test repetitions. As a result, both T_2 and T_2* were calculated in Test Three.

A total of 29 samples were used in Test Three, one of which was a pure water sample. Of the 29, only 24 were newly created samples (Figure 4.6). The remaining 4 were existing samples from Test One, selected to prove if there were any loss in magnetization of the SPIO nanoparticles over a long period of time. Test tube samples were randomly distributed to measure potential effects of sample interaction and their relaxation time changes based on their test tube rack position. Test Three SPIO nanoparticle concentration range spanned over the entire concentration range utilized in both Test One and Test Two. Each of the samples prepared for Test Three were measured to contain similar SPIO nanoparticle quantities as samples used in the previous two tests.

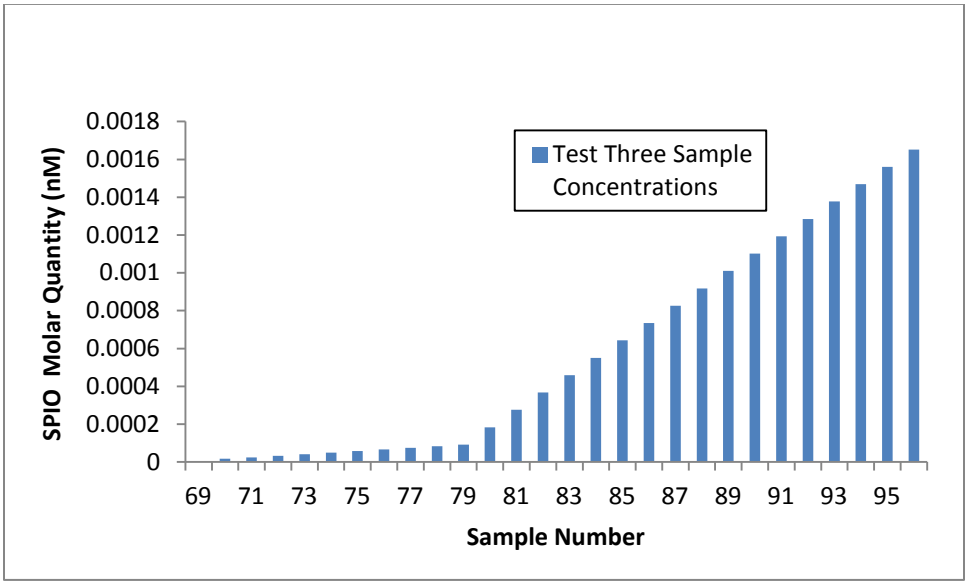

Figure 4.6 Test Three sample's SPIO nanoparticles molar quantities

Using the SPIO nanoparticle concentration versus T_2 data, the Test One SPIO nanoparticle concentrations were re-fitted to their expected values with respect to their individual T_2 times. A trend line was fitted to the Test Three T_2 versus SPIO nanoparticle particle concentration data. The T_2 values of each sample for the Test One data

were plotted along this curve to determine their predicted SPIO nanoparticle concentrations. The newly calculated SPIO nanoparticle concentrations for Test One more accurately fit than what was previously measured.

4.4 Test Four: T_2 as a Detection Mechanism

The primary purpose of Test Four was to prove that T_2 could be used to detect the presence of biotinylated polystyrene (BPM) particles. The biotin coated polystyrene (BPM) particles were ordered from Spherotech. These particles were 3-3.4µm in size with $4.96*10^5$ Streptavidin-FITC binding sites available per polystyrene particle.

There were 42 samples total in Test Four, with one being a pure water sample. From the T_2 versus SPIO nanoparticle concentration found in Figure 4.7, two sample concentrations were selected to be used for the detection mechanism. These two sample concentrations were selected based on their position on the T_2 versus concentration curve where slight changes in magnetic environment could greatly alter the T_2 values. It was predicted that these SPIO nanoparticle concentrations would show the most noticeable change in their T_2 values after the addition of the BPM particles.

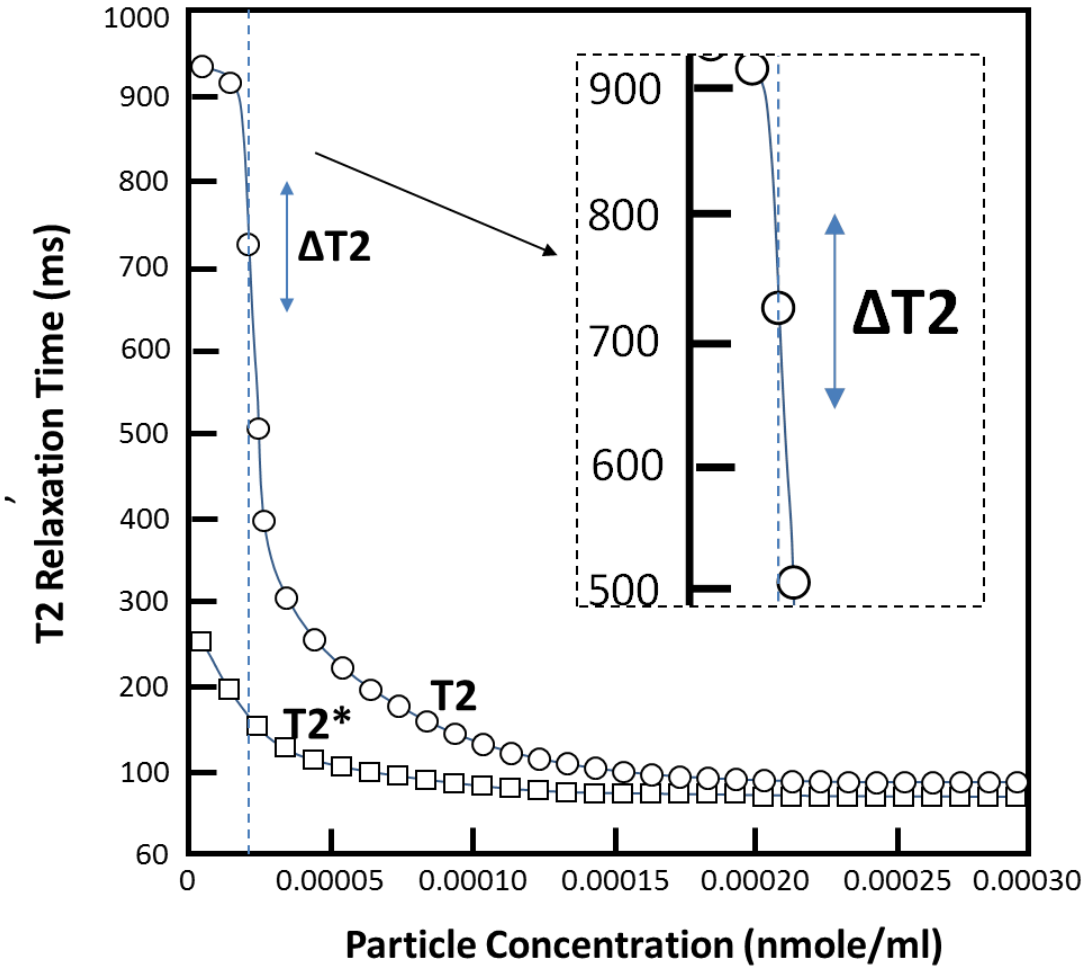

Figure 4.7 Diagram indicating the predicted changes in T_2 values after the addition of the target molecules. The resultant change in T_2 was predicted to show a larger deviation for IO concentrations along the upward portion of the curve shown above.

The sample SPIO nanoparticle concentrations chosen were from sample numbers 79 and 80. Of the 41 SPIO nanoparticle samples, 2 contained only SPIO nanoparticle concentrations samples number 79 and 80, respectively. The remaining 39 samples were divided into 20 containing only sample number 79's concentration and 19 with only sample number 80's concentration. Later, the biotinylated polystyrene particles were added in specific concentrations to these 39 samples. After the addition of the biotinylated polystyrene (BPM) particles, the samples were sonicated to support biotin-streptavidin interaction.

Table 4.2 Sample 79 and 80 SPIO nanoparticle molar concentration

Sample	SPIO Molar concentration
79	.0000918 nM
80	.0001836 nM

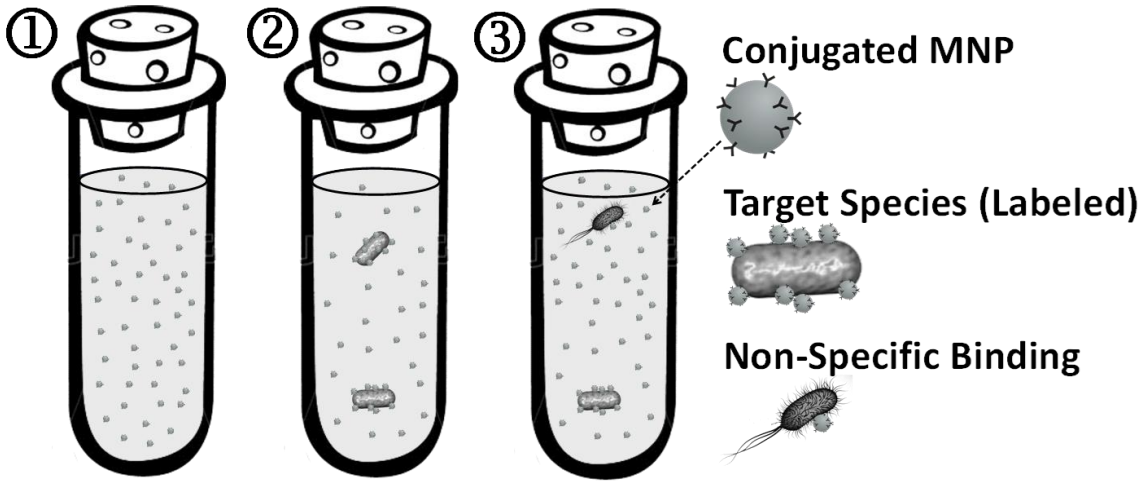

Figure 4.8 Diagram representing the expected binding between the SPIO nanoparticles coated with streptavidin and the biotinylated polystyrene microspheres. (1) The samples are originally formed with only dionized water and the desired SPIO nanoparticle concentration. (2) The samples are later combined with a specific concentration of the biotinylated polystyrene microsphere (BPM). The resultant change in T_2 will be calculated in order to provide proof of the method as a detection mechanism. (3) Non-specific binding of the SPIO nanoparticles could potentially influence the accuracy of the relaxation time measurements.

The addition of the biotinylated polystyrene microspheres to the samples containing the SPIO nanoparticles was expected to bind together forming SPIO-BPM clusters. The formation of these clusters was predicted to induce larger local magnetic field inhomogeneities, thereby shortening the spin-spin relaxation rate (smaller T_2) of surrounding water proton spins. The resultant change in spin-spin relaxation (T_2) due to the addition of these microspheres would verify this method as a detection mechanism (Figure 4.8).

The biotinylated polystyrene particles added to the 39 samples were over a range of 1µl to 100µl (253000 microspheres/ µl) to determine the minimum concentration for detection. Each BPM concentration was repeated twice to assure its test reliability. The testing was divided into two parts (Figure 4.9), samples containing only SPIO nanoparticle concentrations used in sample number 79 and those with only concentrations from sample number 80. One sample from each test part contained pure water and the specific SPIO nanoparticle concentration of sample numbers 79 and 80. The remaining samples for both Test Four parts were combined with increasing amounts of BPM particles listed in Table 4.5. The samples were all sonicated for 20 minutes and stored overnight. Finally, after 24 hours, the Test Four samples were tested for their T_2 values.

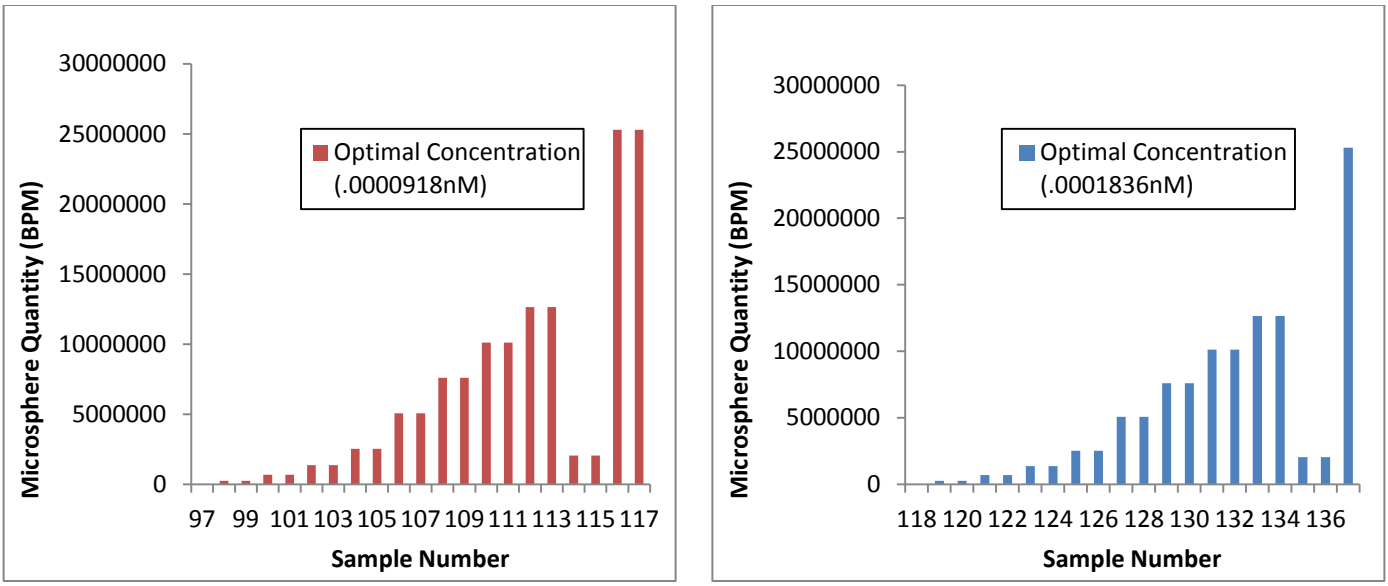

Figure 4.9 Displays the polystyrene microsphere (BPM) count within each sample number with its respective SPIO nanoparticle optimal concentration

After the MRI scan and data reduction, the T_2 values for samples containing biotinylated polystyrene particles were compared to the T_2 value of their respective SPIO nanoparticle concentration without the polystyrene additions. This value would provide the ΔT_2 value for each of the biotinylated polystyrene samples. The ΔT_2 value was predicted to show proof of the existing BPM particle concentrations in each of the samples [4, 5, 6]. ΔT_2 was calculated as follows:

$$\Delta T_2 = T_2(\text{original}) - T_2(\text{detection})$$

T_2(original) = MNP concentration without polystyrene bead

T_2(detection) = MNP concentration with polystyrene bead

4.5 Test Five: Detection at a Higher SPIO Nanoparticle Concentration

After discussing the results of the previous test it was concluded that the detection needed to perform at a higher SPIO nanoparticle concentration to assure the unexpected T_2 values from Test Four were due to limited SPIO-BPM interaction. There were 12 new samples created for Test Five (Figure 4.10). Of these 12 new samples, 1 was a pure water sample and 2 were samples containing only the SPIO nanoparticle concentration selected. The SPIO nanoparticle concentration selected for Test Five was of the same molar concentration (0.0002754nM) as

sample number 81 from Test Three. This was to compare the consistency the T_2 values between Tests Three and Five. The molar concentration was also chosen to be of a higher value than that use in Test Four.

All but the pure water sample, were filled with the same SPIO nanoparticle molar concentration of 0.0002754nM. After the addition of the SPIO nanoparticles, increasing concentrations of the polystyrene microspheres (BPM) were added to 9 of the 12 new samples. The concentration of the BPM added were of the same values as what was added to each test tube in Test Four for data comparison. Unlike Test Four, the samples from Test Five were sonicated 30 minutes prior MR imaging.

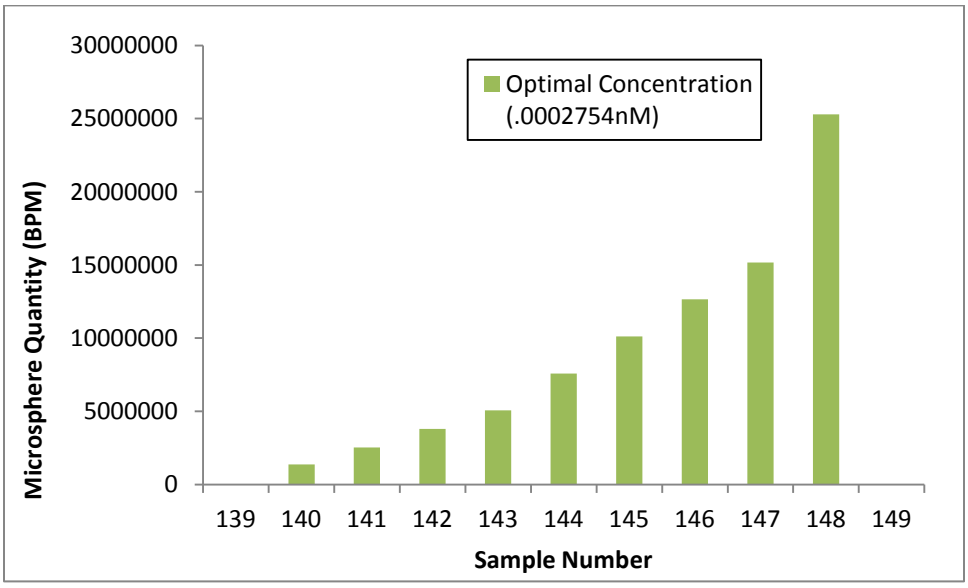

Figure 4.10 Polystyrene microsphere (BPM) count within each sample number with its respective SPIO nanoparticle optimal concentration

After the data reduction of the Test Five data, the ΔT_2 of the new samples were calculated. The new ΔT_2 data was then compared to the ΔT_2 values from the previous test to determine if there was any trend with the T_2 values and the increasing additions of polystyrene microspheres (BPM).

4.6 Test Six: Confirmation of the T_2 Values with Increasing BPM Concentration

To verify the T_2 values measured from Test Five, an additional test was performed. Test Six included 30 new samples and the 12 samples from Test Five (Figure 4.11). The 30 new samples each contained the same SPIO nanoparticle molar concentration that was used from Test Five (0.0002754nM). After the addition of the SPIO nanoparticle to each sample, the polystyrene microspheres (BPM) were then combined with the new samples in

the same increasing concentration as what was used in Test Five. Each BPM addition was repeated 3 times in order to insure accurate data.

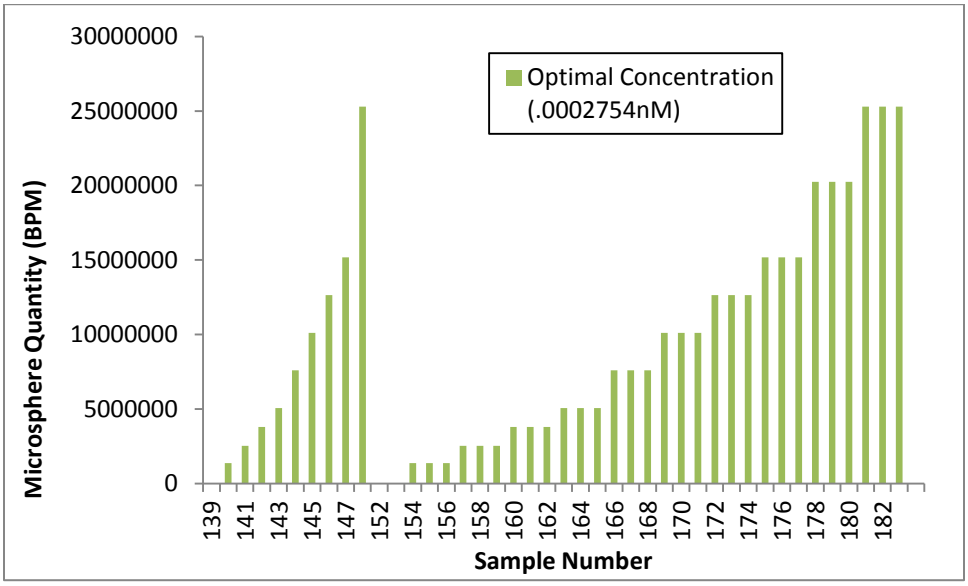

Figure 4.11 Polystyrene microsphere (BPM) count within each sample number with its respective SPIO nanoparticle optimal concentration. The samples used in Test Five were retested to verify the repeatability of their T_2 values.

All samples were sonicated 24 hours prior to MR imaging and were randomly distributed along the test tube rack. Finally, after data reduction, the ΔT_2 was calculated for each sample.

4.7 Test Seven: Determining Particle Settling Using Sagittal Imaging

In the preceding test it was verified that a visible precipitate formed over the course of the MRI scanning sequence. Due to the larger micron size of the polystyrene spheres, it was believed that during the formation of the SPIO-BPM clusters, the aggregates would become too dense and settle to the bottom of samples. To confirm whether this phenomenon was occurring during the scanning procedure, two sagittal slices were taken of each of the test tubes for Test Seven.

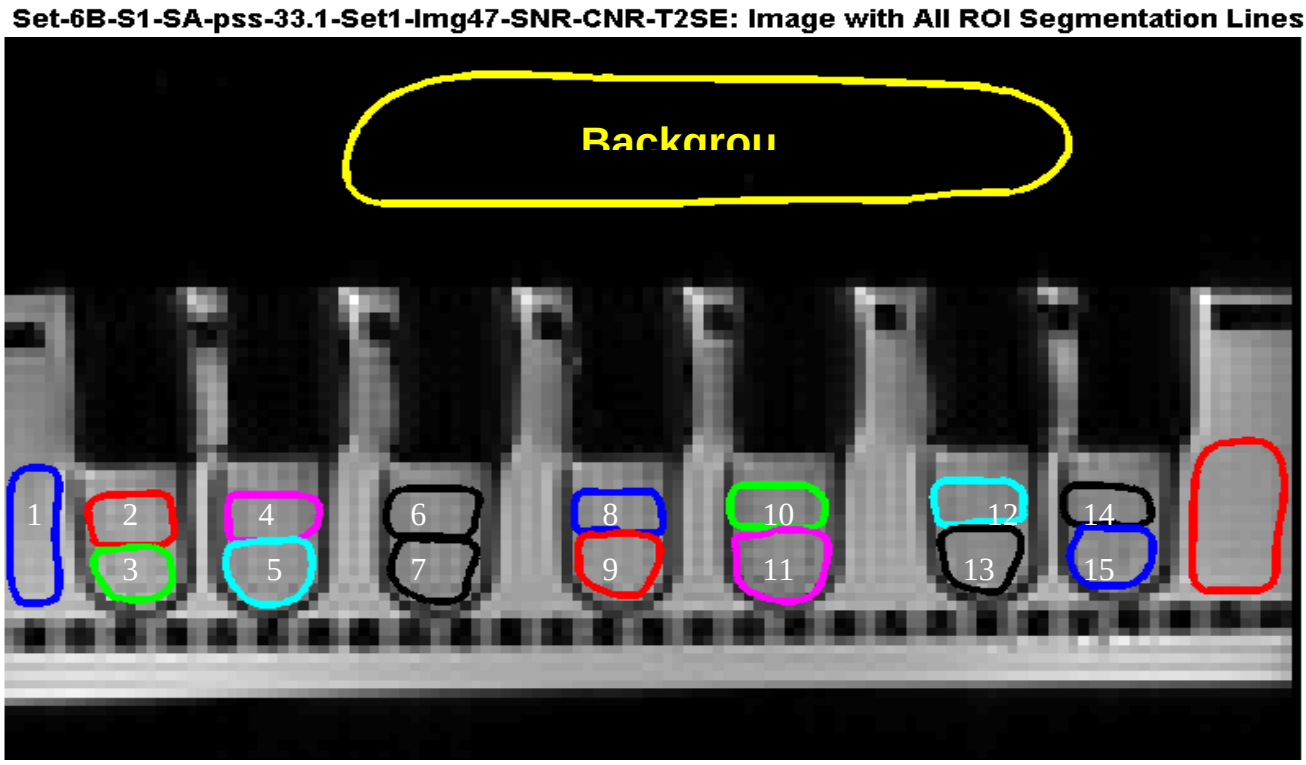

Figure 4.12 MRI of the sagittal slices taken of the first column of test tubes within the rack prior to the scanning sequence.

In order to compare the consistency of the T_2 values for Test Six and Seven, the samples from Test Six (Figure 4.11) were reused. All samples were sonicated 5 minutes prior to the start of the MRI sequence to ensure as little settling as possible. As shown in Figure 4.12, a sagittal slice of the top and bottom of the samples were taken throughout the imaging over a period of 48 hours. The samples remained within the MRI's 3.0 Tesla field during the 48 hour imaging procedure. Each of the six columns shown below in Figure 4.13 was tested over a total acquisition time of 8 hours. Since it was unknown when the particle settling would occur, each of the columns from Figure 4.13 were tested individually starting from the far left column then proceeding with next adjacent column to the right. The far left column was tested during the start of the scanning sequence until 8 hours later after its acquisition time was completed while the far right column was tested after 40 hours under the magnetic field until 8 hours later its own acquisition time was completed.

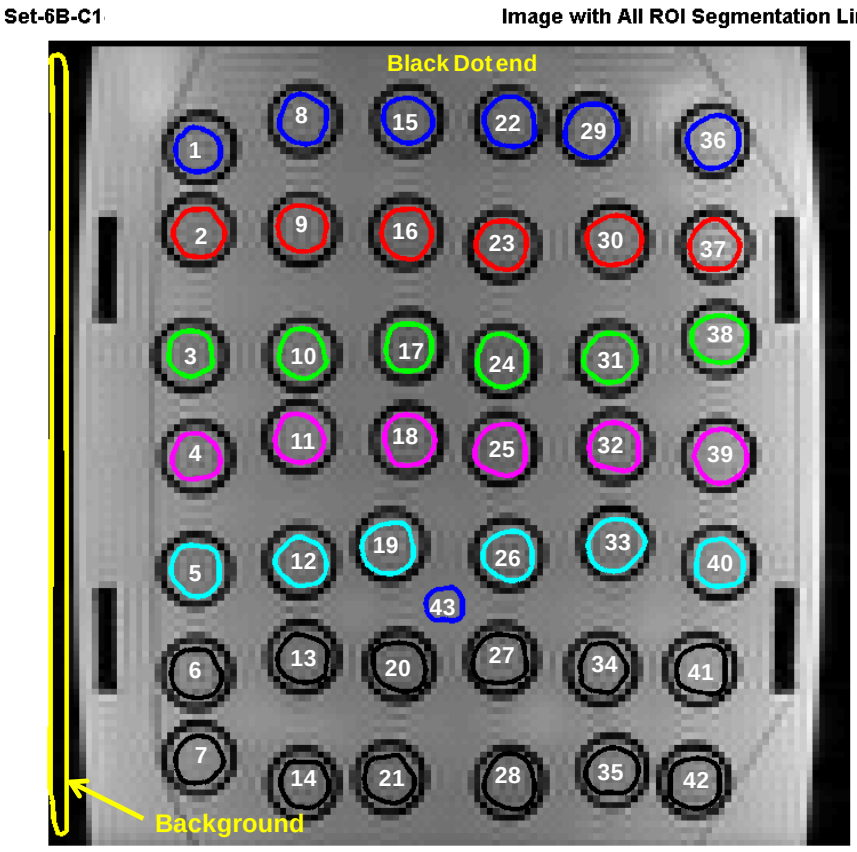

Figure 4.13 Locations of each of the samples in the test rack from an aerial view. The colored circled regions are the areas targeted for their T2 signal during their acquisition time. Numbers 1-10 from the image above correspond to the sample numbers 139-148 while numbers 11-14 are samples 151-154. Finally the above numbers 15-42 parallel the samples 162-182.

CHAPTER 5

RESULTS and DISCUSSION

5.1 Relaxation Time and Particle Size Comparison

It has been reported previously that by differing the core size of the SPIO nanoparticles, noticeable changes in the relaxation rates of the surrounding water molecules would occur [4, 5, 6, 17]. In the first test, two different IO core sizes were used to monitor their respective influences on the T_1, T_2, and T_2* of the water molecules. The findings of Test One showed that the 30 nm SPIO nanoparticle tested with a greater effect on the changes of T_1, T_2, and T_2* than the smaller 10 nm SPIO nanoparticle. It was theorized that although the reduction of the core would decrease the magnetic domain size of the particle, the magnetic field surrounding the particle would also be condensed to a point where the influence would not be great enough until higher concentrations of the particle were used. In Figure 5.1, a comparison of the different SPIO particle core sizes and their impact on T_1, T_2, and T_2* is shown below.

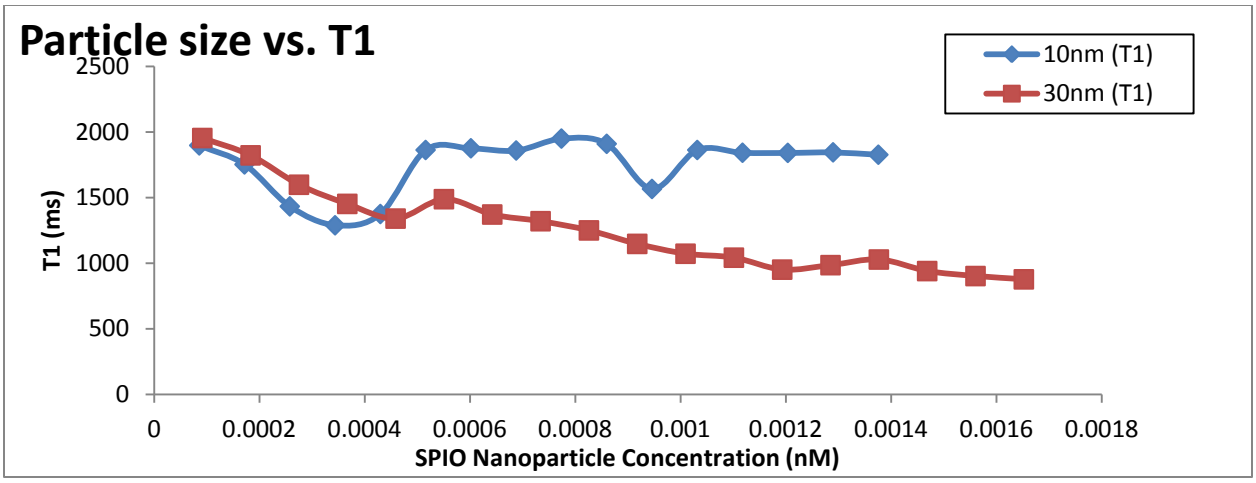
Particle size vs. T1
10nm (T1)
30nm (T1)
T1 (ms)
2500
2000
1500
1000
500
0
0
0.0002
0.0004
0.0006
0.0008
0.001
0.0012
0.0014
0.0016
0.0018
SPIO Nanoparticle Concentration (nM)

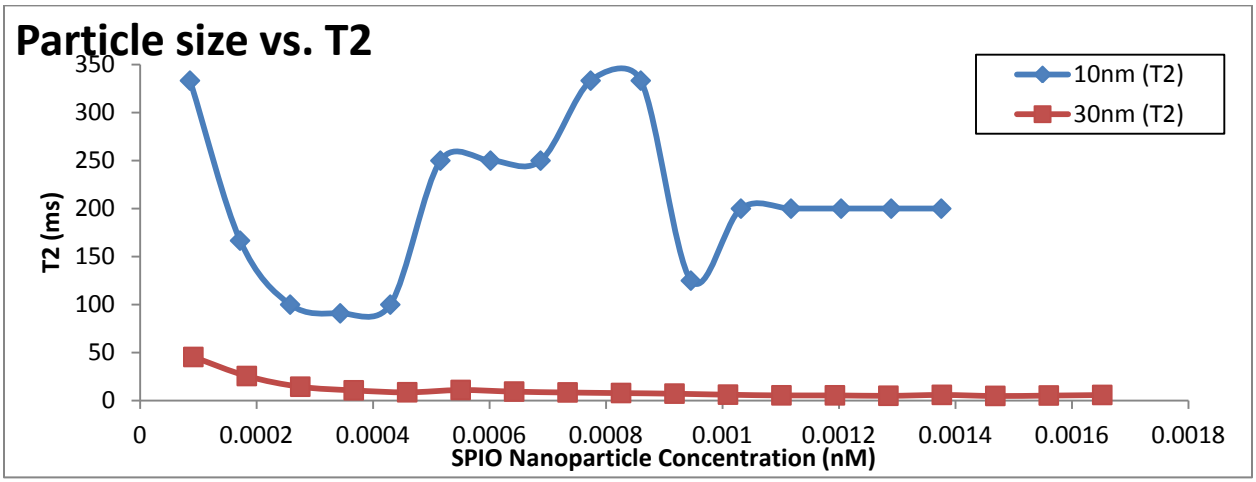
Particle size vs. T2
10nm (T2)
30nm (T2)
T2 (ms)
350
300
250
200
150
100
50
0
0
0.0002
0.0004
0.0006
0.0008
0.001
0.0012
0.0014
0.0016
0.0018
SPIO Nanoparticle Concentration (nM)

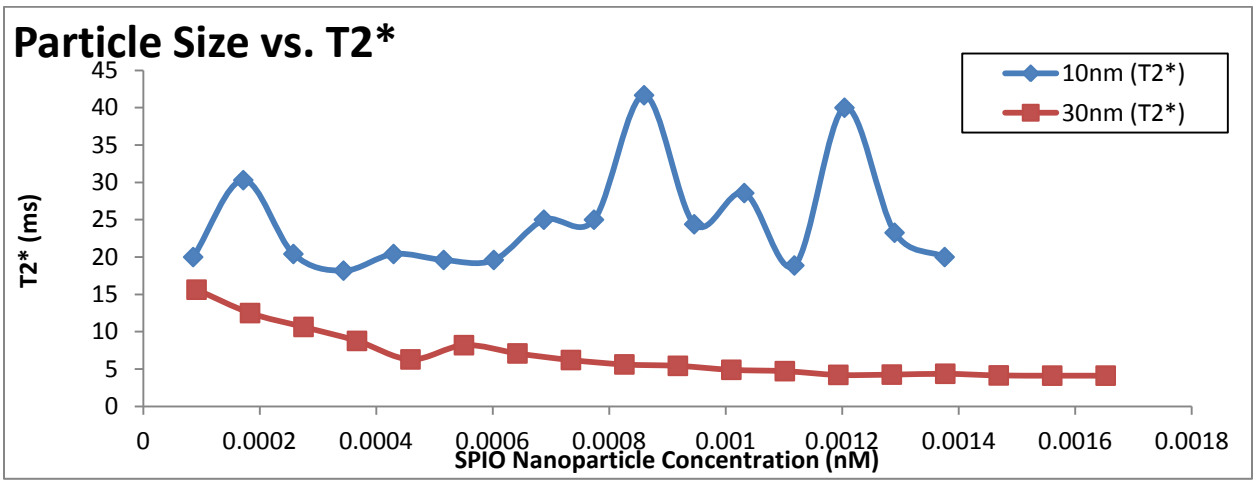
Particle Size vs. T2*
10nm (T2*)
30nm (T2*)
T2* (ms)
45
40
35
30
25
20
15
10
5
0
0
0.0002
0.0004
0.0006
0.0008
0.001
0.0012
0.0014
0.0016
0.0018
SPIO Nanoparticle Concentration (nM)

Figure 5.1 Test One: top (a), middle (b), and bottom (c) graphs display the varying changes in T_1, T_2, T_2* associated with particle size and concentration

It was also verified from Test One that the presence of the SPIO nanoparticles in the solution had little to no effect on the values for T_1. Any of the particle concentration dependencies of the longitudinal magnetization fluctuations seemed to follow no trend and were of similar values as the pure water samples. In Figure 5.2 it can be seen that the values for T_2 and T_2* were of a much smaller magnitude than that of T_1 for all sample concentrations and particle sizes. This finding followed other research previously mentioned and was decided that T_1 would not be the essential variable for further development of the detection mechanism.

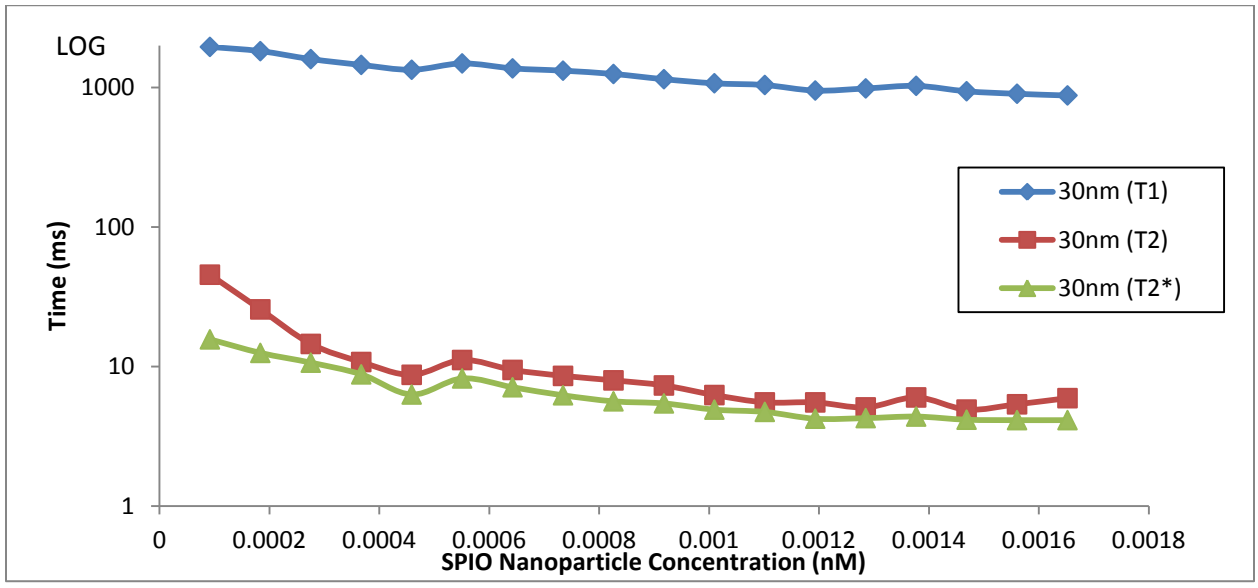

Figure 5.2 Test One: comparison of the 30nm SPIO nanoparticles proton relaxation data

Following this judgment, further testing would include an expanded range of the SPIO nanoparticle concentrations to determine if any related T_2 and T_2* changes would follow a specific trend. This trend would potentially allow for discovery of the optimal SPIO nanoparticle concentration for target detection.

5.2 Reliability of T_2 and T_2*

As can be seen from Figure 5.4 the Test Two measured values for T_2* of the 30nm SPIO particle concentrations did not follow the expected trend theorized for the lower concentrations of the SPIO nanoparticles. The values were found to be highly disordered and were greatly influenced by any external interactions or particle aggregation. T_2* was severely affected by any disturbances in the magnetic field. Any inhomogeneities in the

magnetic field would alter the expected trend in the T_2* vs. concentration. As shown in Figure 5.3 (a), the equilibrium position of the transverse directional component is aligned in the direction of the spectrometers static magnetic field (B_0). Once the RF excitation pulse is applied, the transverse component will transition to the direction of the applied pulse (B_1). The relaxation period (T_2) for the decay of this directional component from the RF excitation pulse induced excited state to the equilibrium position, Figure 5.3 (b) and (c), is dependent on the strength of the magnetic field (B_0) [8]. Unlike T_2, the local magnetic environment (T') greatly manipulates T_2*. This can be seen from Eq.4 where the variable T' is strongly dependent on any surrounding magnetic disturbance. The inhomogeneity factor (T') considers the influence of the magnetic moments of surrounding molecules on the water hydrogen proton's transverse magnetization directional component (T_2) [8, 9]. The local magnetic dipoles enhance the decay of the hydrogen proton's transverse magnetization along with the external field thereby shortening the relaxation period [8].

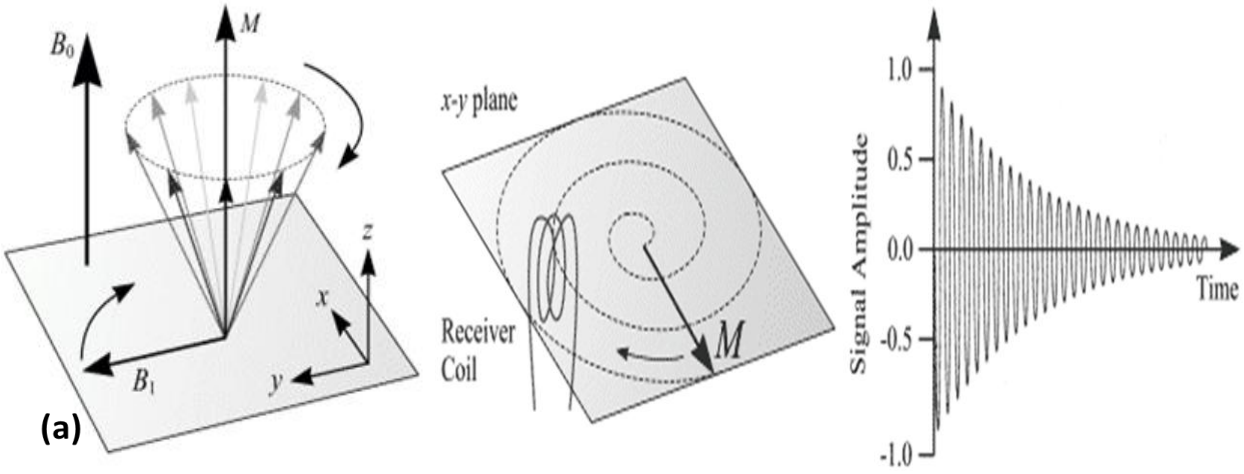

Figure 5.3 Left (a), water hydrogen proton's dipole moment is aligned with spectrometers static magnetic field (B0). The directional component is changed to B1 after RF excitation pulse. Middle (b), decay of water hydrogen protons transverse magnetization directional component. Right (c), NMR signal acquired by spectrometer over transverse relaxation period [25].

The observed frequency collected is highly dependent on the variation of the magnetic field as it transitions through the NMR tube. Any fluctuations in the magnetic field would effectively alter this frequency thereby broadening the NMR line (Figure 5.3 c). As demonstrated in Eq.4 this broadening effect is directly proportional to the frequency and the inhomogeneity of the magnetic field. Considering that the SPIO particle dispersion in the targeted area for imaging would be of differing concentrations for each sample, it was predicted that T_2* could not be used as a detection mechanism. Although the data suggests that at higher concentrations of

SPIO nanoparticles, the average values of T_2* appear to remain consistent, it may still not remain dependable for larger volume samples.

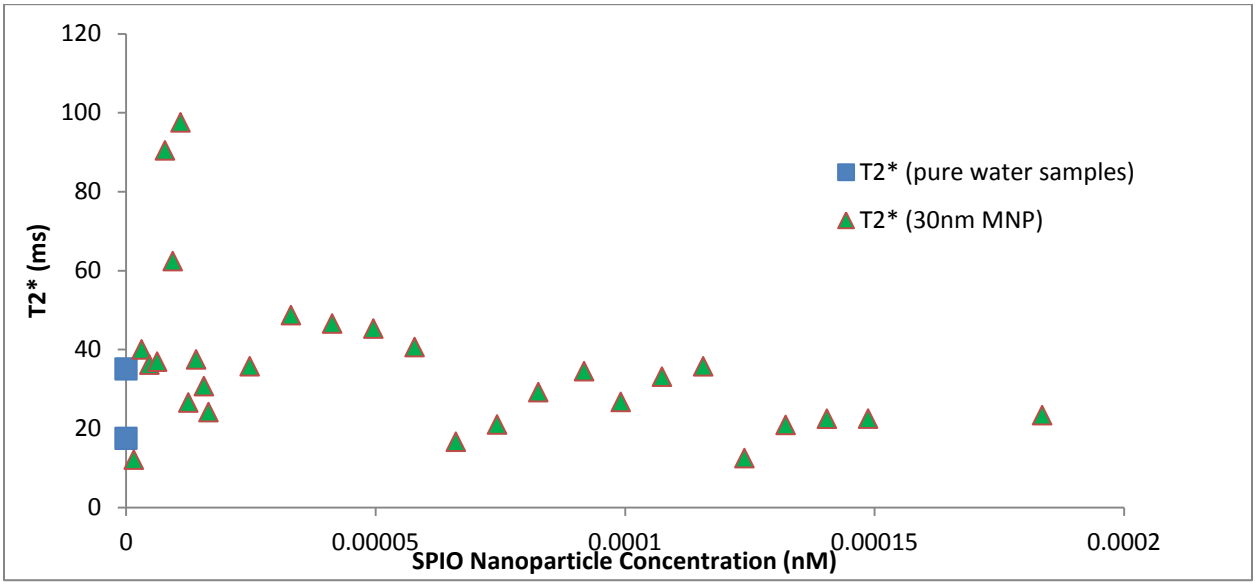

Figure 5.4 Test Two: calculated T2* values for the 30 nm SPIO nanoparticles.

Due to the inconsistencies found from the T_2* data collected from Test One and Two, it was considered necessary to determine if any exterior effects were disturbing the acquired NMR signal. Multiple modifications to the setup were made for Test Three in order to demonstrate T_2*'s variations. First, it was believed that the magnetic fields within each sample could feasibly alter the received signal from any adjacent sample. This was tested by randomizing the particular order of the samples in the rack and examining any changes in relaxation rates from samples that were in close proximity of higher SPIO nanoparticle concentrations. The theory was found to be disproven due to the lack of any particular patterns that would suggest these influences. Second, the experimental setup was examined for any possible contaminations that would inhibit the NMR signal. The test tubes, pipettes, and test tube rack were all inspected prior to Test Three and were all confirmed to be clean. The T_2* data for the lower concentrations in Test Three, shown in Figure 5.5, was also found to be disordered.

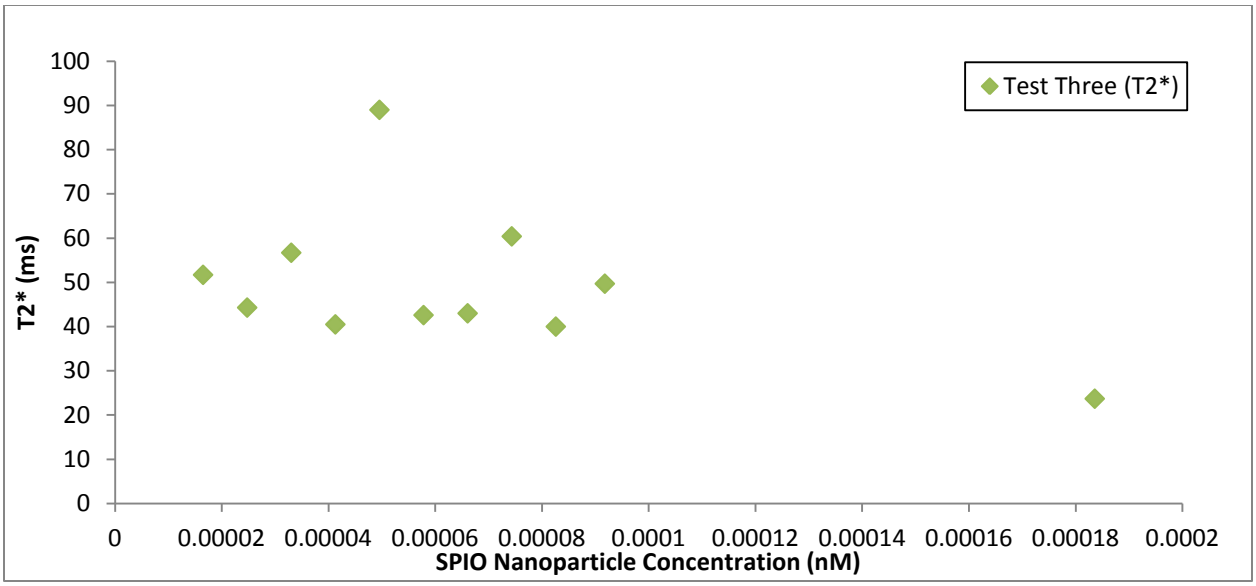

Figure 5.5 Test Three: Lower concentrations of the SPIO nanoparticles were retested for their T2* values in Test Three to determine the consistency between Test Two and Three values.

Third, the effect of the NMR signal transitioning between the water bath, test tube, and sample solution was reviewed. It was believed that the route taken by the signal through alternating mediums could potentially hinder its reception and reduce the signal-to-noise ratio. The samples from Test One were retested for their T_1, T_2, and T_2* values when imaged without the water bath during the imaging sequences. A variance in T_2* between the tests with and without the water bath can be seen in Table 5.1. However, this variance could not be verified to be influenced by the water bath since there were many other factors that could cause the indicated discrepancies. More importantly the water bath data shows a more consistent result that match predictions while the without water bath has more outliers.

Table 5.1 Wet-to-Dry Percentage Change in T_2*

Sample Number	30nm SPIO Molar Quantity (nM)	Wet (With WB)	Dry (Without WB)	% Change T_2*
1	0.0000918	14.16	15.73	11.09
2	0.0001836	12.82	17.75	38.48
3	0.0002754	9.63	12.14	26.08
4	0.0003672	8.02	9.22	14.87
5	0.000459	6.16	7.29	18.28
6	0.0005508	7.91	8.48	7.21
7	0.0006426	6.27	7.64	21.85
8	0.0007344	5.95	6.92	16.32
9	0.0008262	5.60	6.92	23.40

10	0.000918	5.27	5.91	12.16
11	0.0010098	4.73	5.06	6.84
12	0.0011016	4.46	4.89	9.76
13	0.0011934	3.89	4.02	3.32
14	0.0012852	3.97	4.32	8.89
15	0.001377	4.06	4.62	13.76
16	0.0014688	4.08	4.32	5.83
17	0.0015606	3.90	4.07	4.36
18	0.0016524	3.83	3.89	1.51
19	0	38.95	27.83	-28.55
20	0	20.57	40.07	94.84
Sample Number	10nm MNP Molar Quantity (nM)	Wet (With WB)	Dry (Without WB)	% Change T_2*
21	0.000086	17.97	34.69	92.99
22	0.000172	28.08	28.87	2.82
23	0.000258	21.32	29.60	38.80
24	0.000344	20.35	29.18	43.36
25	0.00043	22.49	25.00	11.15
26	0.000516	20.70	23.29	12.51
27	0.000602	20.23	22.42	10.84
28	0.000688	22.76	33.42	46.86
29	0.000774	23.44	34.98	49.24
30	0.00086	39.56	35.27	-10.83
31	0.000946	26.71	18.84	-29.48
32	0.001032	28.65	20.90	-27.05
33	0.001118	21.34	21.32	-0.10
34	0.001204	40.15	17.97	-55.23
35	0.00129	22.07	26.62	20.65
36	0.001376	19.61	39.74	102.58

$$\%Change\ T2^{*} = 100 * \frac{(Dry - Wet)}{Wet}$$

Fourth, it can be seen in Figure 5.6 how any changes in the methodology for data reduction can greatly alter the calculated relaxation rates. It was also proven that the relaxation values were more susceptible to fluctuations when at lower SPIO nanoparticle molar concentrations. This led to the belief that for any acceptable experimentation a standard must be maintain for all data reduction calculations. Sampled data was restricted to uphold a minimum R^2 curve fitting value of .98 and would include all relevant data points until the curve

plateaued. Otherwise, the sample data series would be considered to have too small of a signal-to-noise ratio and be rejected as a suitable calculation.

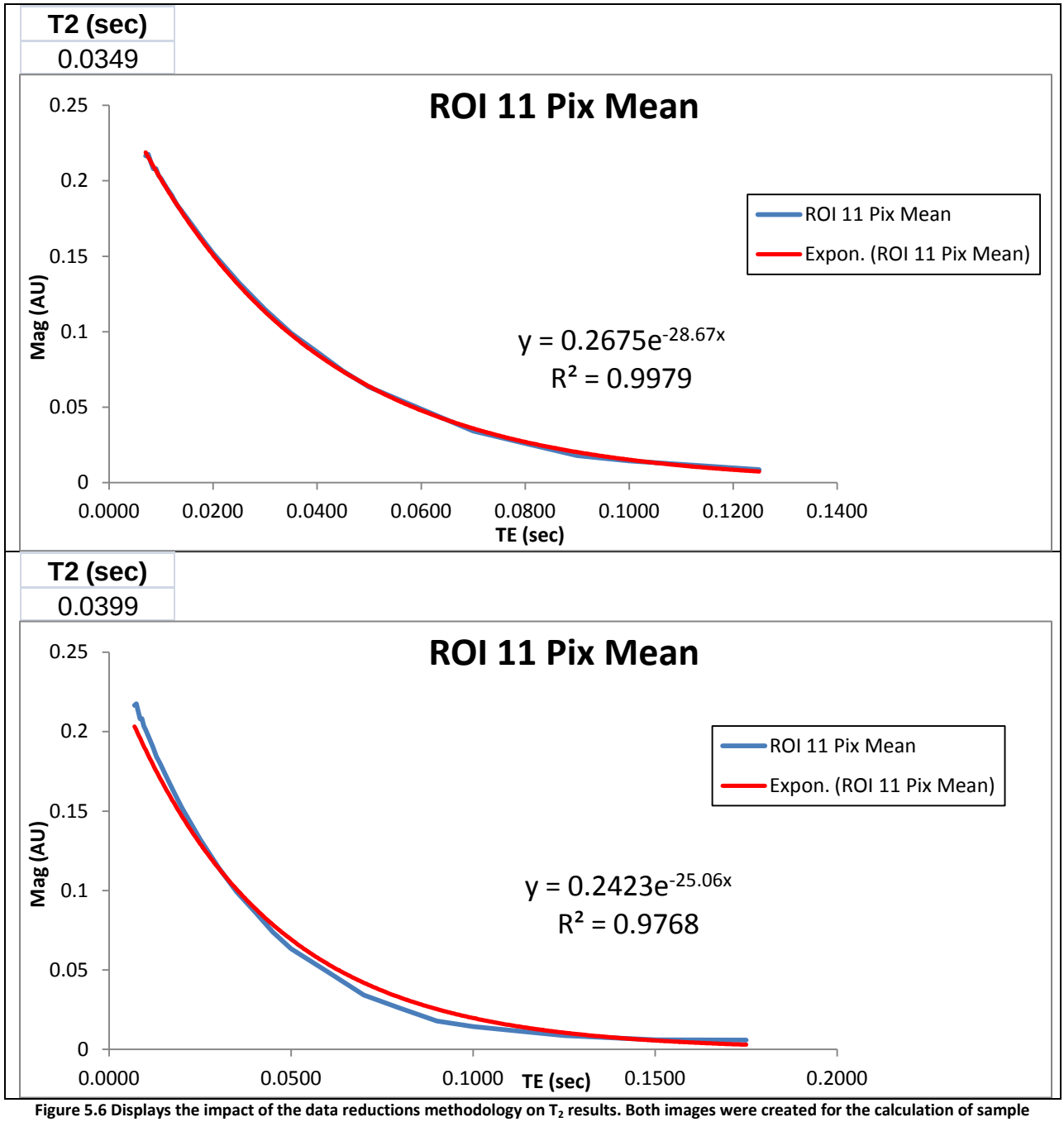

Figure 5.6 Displays the impact of the data reductions methodology on T_2 results. Both images were created for the calculation of sample 149's T_2 value. The top image contains fewer echo times in comparison to the bottom resulting in a more accurately fit curve and shorter T_2 value.

Lastly, in Test Three there were 4 reused samples that were imaged previously during Test One. Both the T_2 and T_2* values of these 4 Test One samples shown in Table 5.2 remained consistent between Tests One and

Three. Another 12 samples were also imaged in Test Three that contained equal SPIO nanoparticle molar concentrations to that of the previous samples used in Test Two. The T_2* results from both of these tests (Figure 5.4 and 5.5) were found to be comparatively erratic.

Table 5.2 Samples from the previous Test One were repeated in Test Three to confirm the reliability of each test to repeat similar results.

Sample Number	Test One T_2 (ms)	Test Three: T_2 (ms)	Test One: T_2* (ms)	Test Three: T_2* (ms)
4	10.75	11.5	8.77	6
5	8.7	10.2	6.29	7
6	11.11	15.6	8.2	8.2
14	5.08	6.01	4.26	4.8

It was concluded that the reliability of T_2* would only remain dependable when at higher concentrations of the SPIO nanoparticles. After comparing the T_2 data from Tests One and Three, it was hypothesized that only T_2 would act as a sufficient variable for target detection.

5.3 Optimal SPIO Nanoparticle Concentration for T_2 Target Detection

The lower concentrations of the SPIO nanoparticles were selected for use in both Test Two and Three in order to determine an "optimal" concentration to be later used for detection of target molecules. The optimal concentration would be the SPIO nanoparticle molar amount at which any modification to the particles dispersion would cause the greatest fluctuation to the resultant change in proton relaxation or ΔT_2. This theory was discussed previously in Chapter 4.4 which contained an image (Figure 4.4) demonstrating the ideal behavior of the transverse relaxation at this molar quantity. Figure 5.7 displays the nanoparticle concentration range that was predicted to be most sensitive to changes in ΔT_2 due to particle dispersion. The suggested molar range follows along the T_2 curve between the SPIO nanoparticle molar concentrations of .0001-.0005nM.

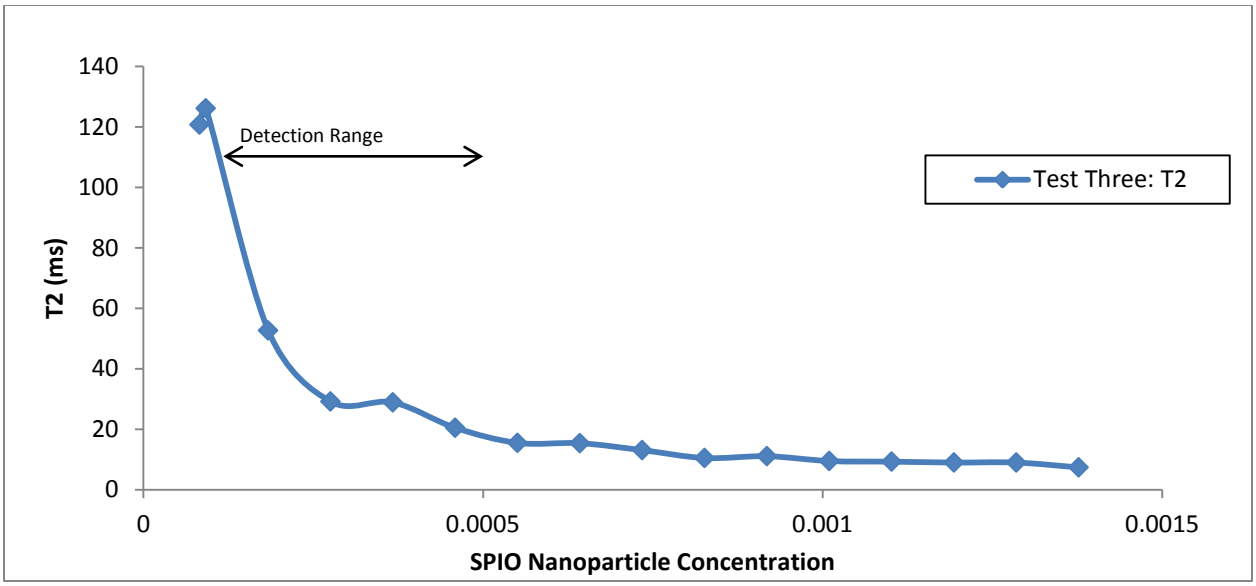

Figure 5.7 Test Three: illustrates the predicted MNP concentration range for detection of the target molecules with greatest sensitivity.

It should be noted that the measured concentrations of the SPIO nanoparticles for Test One were off by a small percentage than from what was originally expected. This was due to a slight malfunction from the pipette that was previously used. All tests following the incident were measured with a properly functioning pipette. The original concentrations for Test One were recalculated based on the trend discovered during Test Three. As shown in Figure 5.7 above, the changes in T_2 follows a tendency that varies directly with the modifications in SPIO nanoparticle concentrations between each solution. Based on this discovery, the previous Test One samples were replaced with newer SPIO nanoparticle concentration values that followed this curve (Figure 5.8). The newly assigned concentrations for Test One samples can be found in Table 7.8 in the Appendix below.

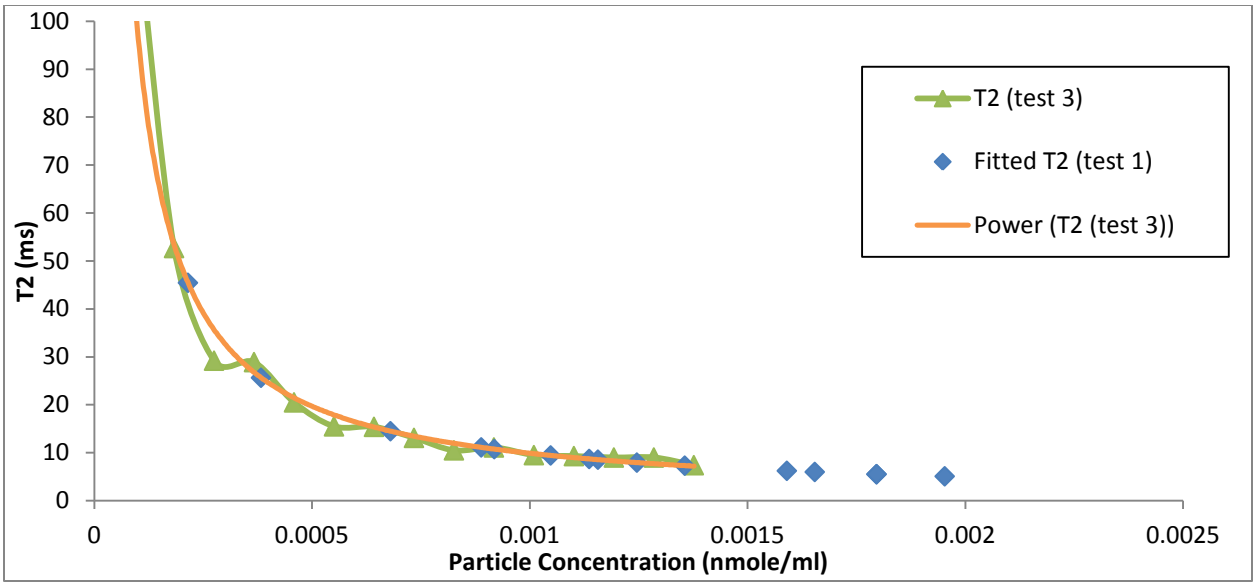

Figure 5.8 Shows the expected values for the Test One sample concentrations based on their recorded T_2 values and the tendency for each SPIO particle concentration to follow the above trend.

5.4 Detection of Polystyrene Microspheres (BPM)

Three molar concentrations within the ideal SPIO nanoparticle molar concentration range were used for SPIO nanoparticle target detection of the polystyrene microspheres (BPM) in Tests Four, Five, Six, and Seven. Originally it was predicted that the most favorable SPIO molar concentrations would be for the lowest quantities in the optimal range. The results obtained from Test Four conveyed a very interesting phenomenon that has not yet been explained in current literature. Unlike in previous reporting, the consequential decrease in transverse relaxation did not occur for all samples upon the addition of the target binding molecule (BPM) with the SPIO nanoparticle. As shown in Figure 5.9a, the data collected from Test Four did not provide the desired indication of T_2 reducing due to particle aggregation for all test samples. The same incident also occurred in Tests Five and Six (Figure 5.9b and 5.9c) when it was decided to use a greater SPIO nanoparticle molar amount. After calculating the ΔT_2 value for each target BPM concentration, the only noticeable pattern was the increase in transverse relaxation with increasing additions of the polystyrene microspheres (BPM).

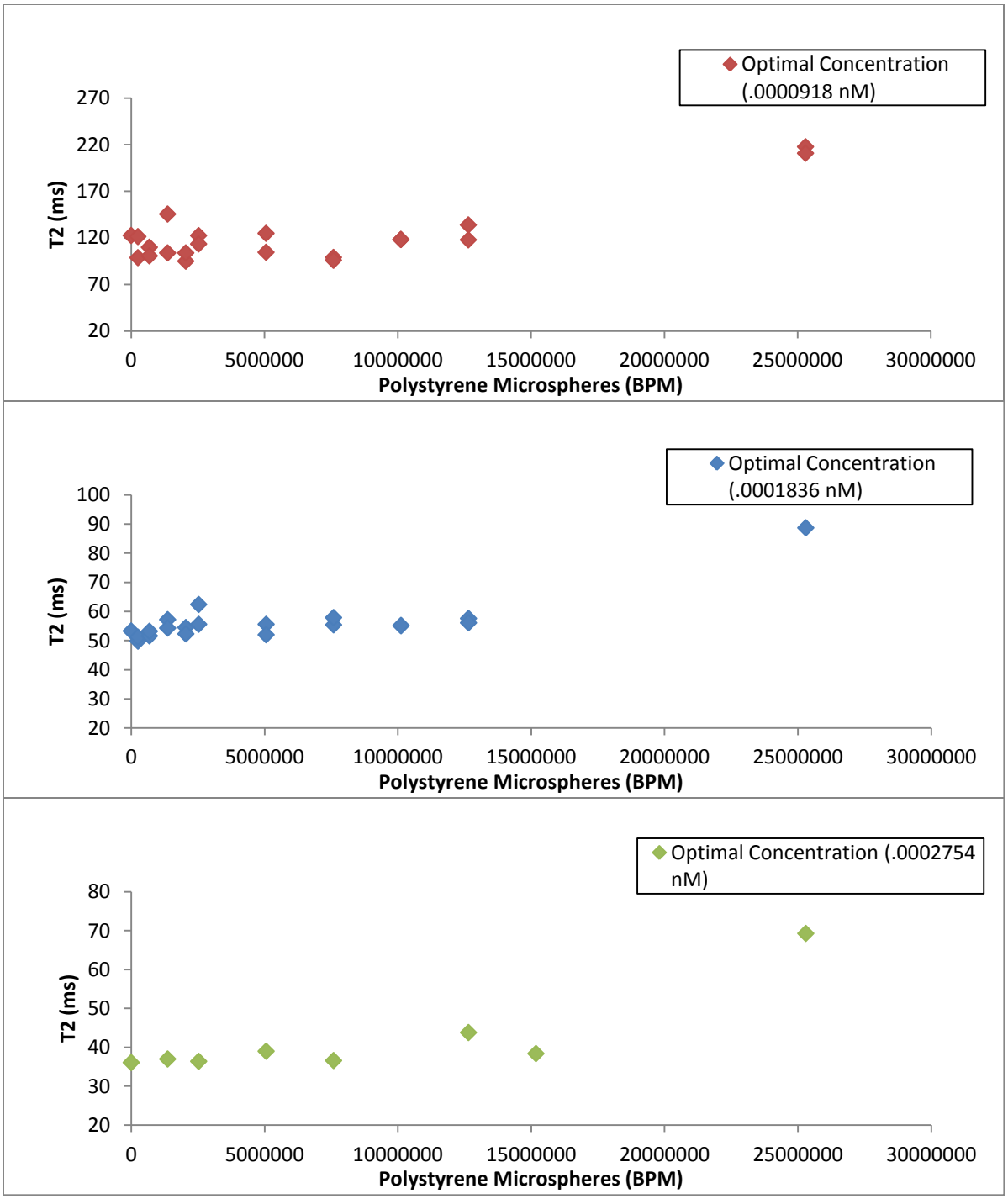

Figure 5.9 The top (a), middle (b), and bottom (c) graphs display the resulting changes in transverse relaxation based on the optimal concentration of the SPIO nanoparticle chosen and the quantity of polystyrene microspheres (BPM) present within the solution.

Although the influence of the BPM augmentation did increase the transverse relaxation time, the T_2 values were not of similar magnitude of that of the pure water samples suggesting that there were still water molecules being impacted by the local magnetic environment. A couple of theories were formulated in order to

explain this phenomenon. First, it was believed that the increase in T_2 was caused by the diffusion of the SPIO nanoparticles to areas of high concentration along the test tube wall when under the applied magnetic field. This would reduce total number of water molecules being affected by the magnetic moments of the SPIO nanoparticles. Although the occurrence would have been encountered in previous testing, it would not have been noticeable until the addition of the polystyrene microspheres (BPM) that would inhibit this diffusional process. Second, there were visible precipitates found for samples containing higher concentrations of the target BPMs. Upon interaction with the SPIO nanoparticles, the target BPMs would form large clusters that would become too dense to remain suspended in solution. The area where the precipitates would form would not be in the space where the coronal slice was imaged along the test tubes. This would also increase T_2 values due to the lessening of water molecules being affected by SPIO nanoparticles.

In response to the first theory, it was demonstrated from Tests One through Six that the samples containing only the SPIO nanoparticles would measure for similar T_2 values between subsequent tests when exposed to an external magnetic field for short periods of time. Alternatively in Test Seven, samples that contained equal SPIO nanoparticle molar concentrations and were not mixed with the polystyrene microspheres (BPM) revealed differing T_2 values when under the MRI's 3.0 Tesla field for prolonged periods of time. Samples 139 and 182 were imaged in Test Seven and contained identical SPIO nanoparticle concentrations without the addition of the target molecules. In Test Seven, the test tubes were placed within the MRI's magnetic field for continuous imaging of 48 hours. Sample 139 was imaged at the beginning of the procedure until the acquisition time completed on the 8^{th} hour while Sample 182 was imaged at the start of the 40^{th} hour until the final acquisition time ended at 48 hours from the start of the test. As shown in Table 5.3, the T_2 value for the Sample 182 was significantly increased after the 40-48 hour period unlike Sample 139. With the data shown Table 5.3 it was reasonable to assume that a portion of the T_2 hindrance discovered in Test Seven was due to the diffusion of the unbound SPIO nanoparticles to highly concentrated areas thus reducing the quantity of water molecules affected by their magnetic dipoles.

Table 5.3 A comparison between the transverse relaxation (T_2) times of two samples containing equal molar quantities of the SPIO nanoparticles. Each sample was imaged at different periods of time while under a continuously applied external magnetic field.

Sample number	Top of test tube T2 (ms)	Bottom of test Tube T2 (ms)	Hours under magnetic field
139	33.8	32.2	0-8hrs
182	67.6	87.3	40-48hrs

To verify the formation of the SPIO-BPM precipitates during MR imaging, a sagittal slice of each test tube was taken in Test Seven in order to image both the top and bottom of the test tubes simultaneously. The procedure was conducted to validate any discrepancy between each images value for T_2. The results of Test Seven indicated that the majority of the samples experienced a lengthening of T_2 at the bottom of samples as a consequence of increasing target concentrations. This effect was most present for samples holding the highest quantities of the BPMs and occurred for each of the columns signal acquisition time periods over the total 48 hours with the exception of the initial 0-8 hour scan. It should also be noted that the T_2 versus BPM concentration dependencies did still follow the previous pattern of increasing with additional concentrations. Figures 5.10 and 5.11 below display the divergences between the T_2 values of top and bottom of the test tubes in Test Seven.

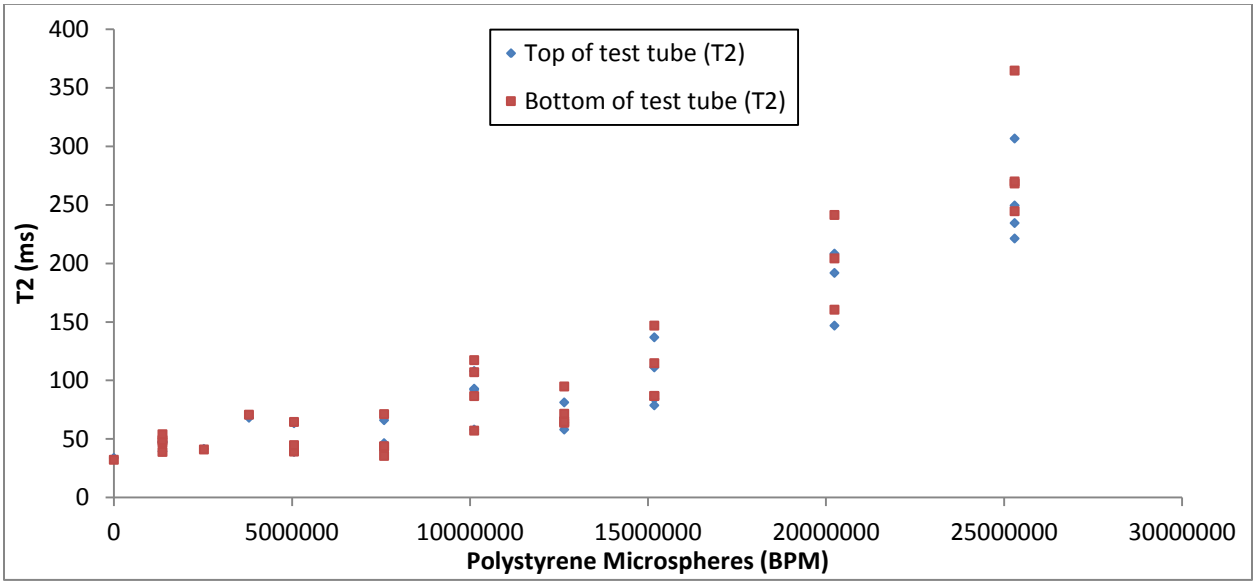

Figure 5.10 Test Seven: displays changes in sample transverse relaxation with differing target BPM concentrations. The top and bottom of each test sample was imaged to determine any variations in T_2 due to particle settling and/or aggregation.

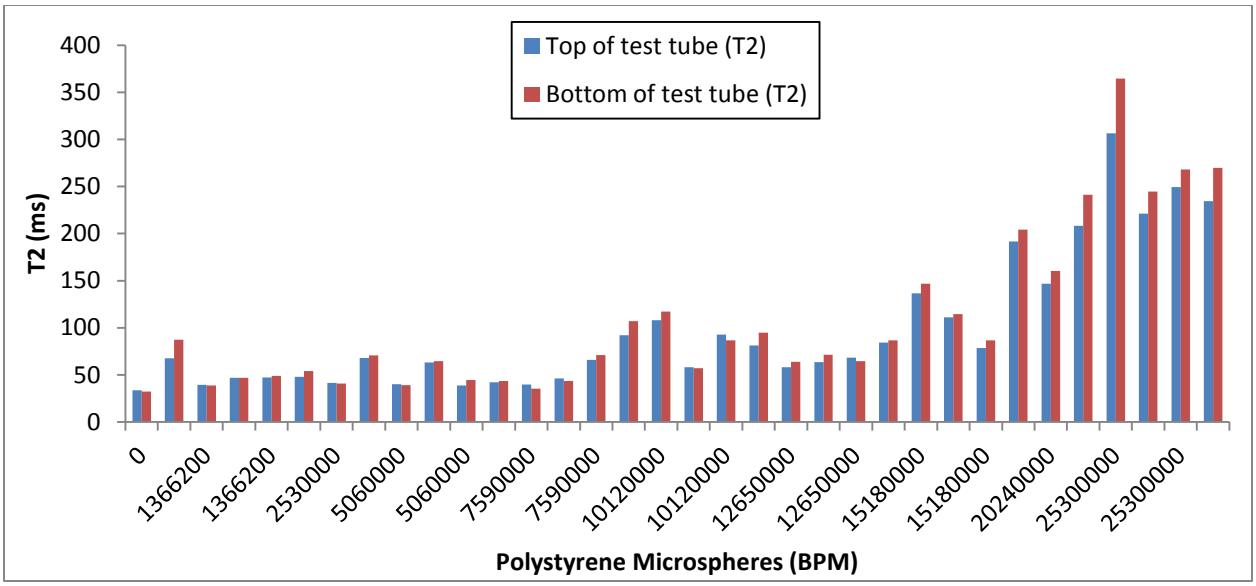

Figure 5.11 Bar graph of Test Seven data for easier visualization of T_2 results.

The greater degree of growth in T_2 for the bottom images than the top images provided an interesting discovery. It was originally predicted that the formation of the SPIO-BPM clusters would consequentially reduce the transverse relaxation (T_2) but was later believed to increase after reviewing the T_2 results from Tests Four, Five, and Six. During these previous tests, the imaging was centralized over the test tube samples thus neglecting the resultant dispersion of the SPIO nanoparticles after mixing. The greater extension of the transverse relaxation for the bottom rather than the top of the test tubes potentially suggests that the target BPM particles size was too large for the predicted T_2 reduction effects to occur. As the accumulation of the SPIO-BPM clusters progresses, the density of the clusters becomes too great to remain suspended within the solution. The transference of the clusters to the bottom of the test tube is initiated thus altering the even dispersion of the molecules. This development would transpire more rapidly for larger micron sized target molecules rather than smaller nanoparticles. The coupling of the SPIO nanoparticle magnetic moments due to SPIO-BPM clustering has been shown in Test Seven to have been inhibited rather than enhanced. The probability of there being multiple SPIO nanoparticles conjugated close enough to each other on the surface of a target molecule (BPM) for the coupling of their magnetic moments to occur, decreases with increasing target molecule size. In previous research that experienced the decrease in transverse relaxation (T_2) due to SPIO-Target clustering typically only targeted nano-sized molecules for detection. This research proposes that there is a maximum target molecule size for NMR

detection when expecting a reduction of T_2 upon the arrangement of the SPIO-BPM clusters. For larger micron sized target particles, Test Seven has shown an alternative method for pathogen detection.

CHAPTER 6

CONCLUSION

This research has demonstrated a potential detection technique that uses superparamagnetic iron oxide (SPIO) nanoparticles for the capture and recognition of target molecules present in biological media. The SPIO nanoparticle core size was shown to have comparatively differing effects when influencing proton relaxation. A broad concentration range of the SPIO nanoparticles was utilized to test their impact on the three relaxation variables T_1, T_2, and T_2* of the surrounding water molecules. The longitudinal relaxation was found to not be affected by the local SPIO nanoparticles while T_2 and T_2* were shown to be greatly influenced. T_2* was later proven to be unreliable between each subsequent test and was therefore determined to not be applied as the primary variable for the detection mechanism.

An optimal SPIO nanoparticle concentration range for the determination of the target pathogen (BPM) in solution was developed. Unlike what was previously predicted, the interaction of the SPIO nanoparticles with the target BPM did not drastically reduce the transverse relaxation (T_2) times but instead increased upon formation of the SPIO-BPM clusters. Repeated tests confirmed varying increases in T_2 along both ends of the BPM concentration range with a noticeable tendency to increase more substantially for the highest BPM quantities.

A visible precipitate (SPIO-BPM clusters) was discovered for all samples containing the larger concentrations of the target BPM molecules. Based on this sighting, the previous BPM concentrations were continuously imaged over a 48 hour period at the top and bottom of the test tubes to verify any particle settling during the scanning procedure. The results indicated that the majority of the samples experienced a lengthening of T_2 at the bottom of samples as a consequence of increasing target BPM concentrations. Upon further inspection it was shown that all unbound SPIO nanoparticles could potentially slowly diffuse together forming highly concentrated areas and the SPIO-BPM clusters could eventually grow too large forcing them to settle to the

bottom of the test tube. Both occurrences would forcibly reduce the average quantity of water hydrogen protons affected by the SPIO nanoparticles magnetic moments thus increasing the transverse relaxation (T_2) time of the solution. Finally it was concluded that for NMR detection of larger micron-sized target molecules in solution, a rise in transverse relaxation was to be expected.

Appendix

Table 7.1 List of Samples used for Test One with their respective SPIO nanoparticle core size and molar concentration

Sample Number	SPIO Nanoparticle Core Size	30nm SPIO Molar Quantity (nM)	10nm SPIO Molar Quantity (nM)
1	30nm	0.0000918	0
2	30nm	0.0001836	0
3	30nm	0.0002754	0
4	30nm	0.0003672	0
5	30nm	0.000459	0
6	30nm	0.0005508	0
7	30nm	0.0006426	0
8	30nm	0.0007344	0
9	30nm	0.0008262	0
10	30nm	0.000918	0
11	30nm	0.0010098	0
12	30nm	0.0011016	0
13	30nm	0.0011934	0
14	30nm	0.0012852	0
15	30nm	0.001377	0
16	30nm	0.0014688	0
17	30nm	0.0015606	0
18	30nm	0.0016524	0
19	Water	0	0
20	Water	0	0
21	10nm	0	0.000086
22	10nm	0	0.000172
23	10nm	0	0.000258
24	10nm	0	0.000344
25	10nm	0	0.00043
26	10nm	0	0.000516
27	10nm	0	0.000602
28	10nm	0	0.000688
29	10nm	0	0.000774
30	10nm	0	0.00086
31	10nm	0	0.000946
32	10nm	0	0.001032
33	10nm	0	0.001118
34	10nm	0	0.001204
35	10nm	0	0.00129
36	10nm	0	0.001376
37	Water	0	0
38	Water	0	0

Table 7.2 Relaxation rates of each sample in Test One

Sample Number	SPIO core size	T1(ms)	T2(ms)	T2*(ms)
1	30nm	1954	45.45	15.63
2	30nm	1822	25.64	12.5
3	30nm	1598	14.49	10.64
4	30nm	1452	10.75	8.77
5	30nm	1340	8.7	6.29
6	30nm	1488	11.11	8.2
7	30nm	1371	9.43	7.09
8	30nm	1320	8.55	6.21
9	30nm	1250	7.94	5.62
10	30nm	1147	7.3	5.43
11	30nm	1072	6.23	4.9
12	30nm	1042	5.52	4.72
13	30nm	951	5.52	4.22
14	30nm	985	5.08	4.26
15	30nm	1028	5.99	4.37
16	30nm	940	4.9	4.15
17	30nm	902	5.35	4.12
18	30nm	877	5.92	4.12
19	Water	2105	1250	41.67
20	Water	2102	1428.57	19.61
21	10nm	1898	333.33	20
22	10nm	1753	166.67	30.3
23	10nm	1433	100	20.41
24	10nm	1289	90.91	18.18
25	10nm	1375	100	20.41
26	10nm	1863	250	19.61
27	10nm	1876	250	19.61
28	10nm	1859	250	25
29	10nm	1950	333.33	25
30	10nm	1910	333.33	41.67
31	10nm	1566	125	24.39
32	10nm	1863	200	28.57
33	10nm	1842	200	18.87
34	10nm	1841	200	40
35	10nm	1845	200	23.26
36	10nm	1827	200	20
37	Water	2114	1428.57	32.26
38	Water	2111	1428.57	28.57

Table 7.3 List of Test Two Samples with their respective SPIO molar concentration.

Sample Number 30nm	30nm SPIO Molar Quantity (nM)	T2* (ms)
39	0	17.53345659
40	0.000016524	24.17494292
41	0.000024786	35.79919487
42	0.000033048	48.74822399

43	0.00004131	46.61648252
44	0.000049572	45.3406074
45	0.000057834	40.6569547
46	0.000066096	16.67018219
47	0.000074358	21.03710934
48	0.00008262	29.23709996
49	0.0000918	34.54834725
50	0.000099144	26.75877179
51	0.000107406	33.15266425
52	0.000115668	35.78062851
53	0.00012393	12.52498074
54	0.000132192	20.9320007
55	0.000140454	22.50352592
56	0.000148716	22.5281837
57	0.0001836	23.40453537
58	0	35.11420547
59	1.5606E-06	12.14952518
60	3.1212E-06	40.05383465
61	4.6818E-06	36.20958199
62	6.2424E-06	36.96113631
63	0.000007803	90.48134242
64	9.3636E-06	62.4342734
65	1.09242E-05	97.57548901
66	1.24848E-05	26.60273035
67	1.40454E-05	37.5276156
68	0.000015606	30.75677022

Table 7.4 List of Test Three Samples with their respective SPIO molar concentration.

Sample Number	30nm SPIO Molar Quantity (nM)	T2*(ms)	T2(ms)
69	0	59.6	2212.4
70	0.000016524	51.7	512.6
71	0.000024786	44.3	430.1
72	0.000033048	56.7	252.3
73	0.00004131	40.5	287.4
74	0.000049572	89	175.2
75	0.000057834	42.6	162
76	0.000066096	43	181.6
77	0.000074358	60.4	130.4
78	0.00008262	40	120.8

79	0.0000918	49.7	126.2
80	0.0001836	23.7	52.7
81	0.0002754	12.8	29.2
82	0.0003672	15.9	28.9
83	0.000459	10.7	20.5
84	0.0005508	12.9	15.5
85	0.0006426	10.7	15.4
86	0.0007344	10.1	13.1
87	0.0008262	8.5	10.5
88	0.000918	7.2	11.1
89	0.0010098	5.8	9.5
90	0.0011016	5.1	9.3
91	0.0011934	6.2	9
92	0.0012852	6.4	9
93	0.001377	5.7	7.4

Table 7.5 List of Test Four Samples with their respective MNP and Polystyrene-biotin microsphere molar concentration.

Sample	SPIO molar concentration (nM)	BPM (µl)	BPM quantity	T2(ms)
97	0.0000918	0	0	122.6
98	0.0000918	1	253000	98.8
99	0.0000918	1	253000	121.4
100	0.0000918	2.7	683100	110
101	0.0000918	2.7	683100	100.7
102	0.0000918	5.4	1366200	145.6
103	0.0000918	5.4	1366200	103.9
104	0.0000918	10	2530000	122.5
105	0.0000918	10	2530000	113.5
106	0.0000918	20	5060000	124.9
107	0.0000918	20	5060000	104.6
108	0.0000918	30	7590000	99.1
109	0.0000918	30	7590000	96
110	0.0000918	40	10120000	118.3
111	0.0000918	40	10120000	118.3
112	0.0000918	50	12650000	133.9
113	0.0000918	50	12650000	117.9
114	0.0000918	8.1	2049300	95
115	0.0000918	8.1	2049300	103.9
116	0.0000918	100	25300000	217.8
117	0.0000918	100	25300000	210.8

118	0.0001836	0	0	53.3
119	0.0001836	1	253000	49.8
120	0.0001836	1	253000	51.2
121	0.0001836	2.7	683100	51.6
122	0.0001836	2.7	683100	53.2
123	0.0001836	5.4	1366200	57.2
124	0.0001836	5.4	1366200	54.3
125	0.0001836	10	2530000	55.6
126	0.0001836	10	2530000	62.4
127	0.0001836	20	5060000	55.6
128	0.0001836	20	5060000	52
129	0.0001836	30	7590000	55.4
130	0.0001836	30	7590000	57.9
131	0.0001836	40	10120000	55.1
132	0.0001836	40	10120000	55.2
133	0.0001836	50	12650000	57.6
134	0.0001836	50	12650000	56.1
135	0.0001836	8.1	2049300	54.5
136	0.0001836	8.1	2049300	52.3
137	0.0001836	100	25300000	88.7
138	0	0	0	822.4

Table 7.6 List of Test Five Samples with their respective SPIO nanoparticle and BPM molar concentration.

Sample	SPIO molar concentration (nM)	BPM (µl)	BPM particle quantity	T2 (ms)
139	0.0002754	0	0	36.1
140	0.0002754	5.4	1366200	37
141	0.0002754	10	2530000	36.4
142	0.0002754	15	3795000	63.4
143	0.0002754	20	5060000	39
144	0.0002754	30	7590000	36.6
145	0.0002754	40	10120000	68.5
146	0.0002754	50	12650000	43.8
147	0.0002754	60	15180000	38.4
148	0.0002754	100	25300000	69.3
149	0.0002754	0	0	34.9
150	0	0	0	1069.5

Table 7.7 List of Test Six Samples with their respective SPIO nanoparticle and BPM molar concentration.

Sample	SPIO molar concentration (nM)	BPM (µl)	BPM particle quantity	T2(ms)

139	0.000275	0	0	35.5
140	0.000275	5.4	1366200	34.8
141	0.000275	10	2530000	43.5
142	0.000275	15	3795000	70.8
143	0.000275	20	5060000	40.9
144	0.000275	30	7590000	43.1
145	0.000275	40	10120000	97.4
146	0.000275	50	12650000	73.1
147	0.000275	60	15180000	76.3
148	0.000275	100	25300000	320.9
151	0	0	0	1416.4
152	0.000275	5.4	1366200	49.4
153	0.000275	5.4	1366200	47
154	0.000275	5.4	1366200	55.8
155	0.000275	8.1	10	75.6
156	0.000275	8.1	10	55.9
157	0.000275	8.1	10	40.3
158	0.000275	8.1	15	88.6
159	0.000275	8.1	15	171.1
160	0.000275	8.1	15	31.1
161	0.000275	8.1	20	58.3
162	0.000275	20	5060000	58.2
163	0.000275	20	5060000	38.3
164	0.000275	30	7590000	36.8
165	0.000275	30	7590000	45
166	0.000275	30	7590000	56.3
167	0.000275	40	10120000	119
168	0.000275	40	10120000	30.8
169	0.000275	40	10120000	47.7
170	0.000275	50	12650000	51.3
171	0.000275	50	12650000	59.9
172	0.000275	50	12650000	56.1
173	0.000275	60	15180000	87.3
174	0.000275	60	15180000	82.6
175	0.000275	60	15180000	63.7
176	0.000275	80	20240000	89
177	0.000275	80	20240000	75.9
178	0.000275	80	20240000	96
179	0.000275	100	25300000	91.1
180	0.000275	100	25300000	101.3
181	0.000275	100	25300000	88.8

182	0.000275	0	0	39.3

Table 7.8 Test One Fitted Concentrations

Sample Number	T2 (ms)	Fitted Concentration (nM)
1	45.45	0.000215428
2	25.64	0.000383195
3	14.49	0.000680402
4	10.75	0.000918773
5	8.7	0.001136716
6	11.11	0.000888825
7	9.43	0.00104821
8	8.55	0.00115678
9	7.94	0.001246207
10	7.3	0.001356152
11	6.23	0.001590591
12	5.52	0.00179649
13	5.52	0.00179649
14	5.08	0.00195307
15	5.99	0.001654713

References

[1] J. Liu, Z. Cao and Y. Lu, "Functional Nucleic Acid Sensors," *Chemical Reviews,* vol. 109, no. 5, pp. 1948-1998, 2009.

[2] P. K. Jain, X. Huang, I. H. El-Sayed and M. A. El-Sayed, "Noble Metals on the Nanoscale: Optical and Photothermal Properties and Some Applications in Imaging, Sensing, Biology, and Medicine," *Accounts of Chemical Research,* vol. 41, no. 12, pp. 1578-1586, 2008.

[3] L. Wang, K. Wang, S. Santra, X. Zhao, L. R. Hilliard, J. E. Smith, Y. Wu and W. Tan, "Watching Silica Nanoparticles Glow in the Biological World," *Analytical Chemistry,* vol. 78, no. 3, pp. 646-654, 2006.

[4] S. Bamrungsap, M. I. Shukoor, T. Chen, K. Sefah and W. Tan, "Detection of Lysozyme Magnetic Relaxation Switches Based on Aptamer-Functionalized Superparamagnetic Nanoparticles," *Analytical Chemistry,* vol. 83, no. 20, pp. 7795-7799, 2011.

[5] H. Lee, E. Sun, D. Ham and R. Weissleder, "Chip-NMR biosensor for detection and molecular analysis of cells," *Nat Med,* vol. 14, pp. 869-874, 2008.

[6] J. M. Perez, L. Josephson, T. O'Loughlin, D. Hogemann and R. Weissleder, "Magnetic relaxation switches capable of sensing molecular interactions," *Nat Biotech,* vol. 20, pp. 816-820, 2002.

[7] L. Anderson, S. Holden, B. Davis, E. Prescott, C. Charrier, N. Bunce, D. Firmin, B. Wonke, J. Porter, J. Walker and D. Pennell, "Cardiovascular T2-star (T2*) magnetic resonance for the early diagnosis of myocardial iron overload," *European Heart Journal,* vol. 22, no. 23, pp. 2171-2179, 2001.

[8] D. Hoa, *Nuclear Magnetic Resonance,* 2009.

[9] J. P. Hornak, *The Basics of NMR,* 1997.

[10] P. A. Hardy and R. M. Henkelman, "Transverse relaxation rate enhancement caused by magnetic particulates.," *Magnetic Resonance Imaging,* vol. 7, no. 3, pp. 265-275, 1989.

[11] H. Duan, M. Kuang, X. Wang, Y. A. Wang, H. Mao and S. Nie, "Reexamining the Effects of Particle Size and Surface Chemistry on the Magnetic Properties of Iron Oxide Nanocrystals: New Insights into Spin Disorder and Proton Relaxivity," *The Journal of Physical Chemistry C,* vol. 112, no. 22, pp. 8127-8131, 2008.

[12] H. Xu, Z. P. Aguilar, L. Yang, M. Kuang, H. Duan, Y. Xiong, H. Wei and A. Wang, "Antibody conjugated magnetic iron oxide nanoparticles for cancer cell separation in fresh whole blood," *Biomaterials,* vol. 32, no. 36, pp. 9758-9765, 2011.

[13] Y. Chu, P. Zhang, J. Hu, W. Yang and C. Wang, "Synthesis of Monodispersed Co(Fe)/Carbon Nanocomposite Microspheres with Very High Saturation Magnetization," *The Journal of Physical Chemistry C,* vol. 113, no. 10, pp. 4047-4052, 2009.

[14] I. Koh and L. Josephson, "Magnetic Nanoparticle Sensors," *Sensors,* vol. 9, no. 10, pp. 8130-8145, 2009.

[15] D. D. Stark, "Hepatic iron overload: paramagnetic pathology.," *Radiology,* vol. 179, no. 2, pp. 333-335, 1991.

[16] A. Senpan, S. D. Caruthers, I. Rhee, N. A. Mauro, D. Pan, G. Hu, M. J. Scott, R. W. Fuhrhop, P. J. Gaffney, S. A. Wickline and G. M. Lanza, "Conquering the Dark Side: Colloidal Iron Oxide Nanoparticles," *ACS Nano,* vol. 3, no. 12, pp. 3917-3926, 2009.

[17] H. Lee, T.-J. Yoon and R. Weissleder, "Ultrasensitive Detection of Bacteria Using Coreâ€“Shell Nanoparticles and an NMR-Filter System," *Angewandte Chemie International Edition,* vol. 48, no. 31, pp. 5657-5660, 2009.

[18] H. G. R. L. I. A. Jaganathan, "Characterizing proton relaxation times for metallic and magnetic layer-by-layer-coated, DNA-templated nanoparticle chains," *Nanotechnology,* vol. 21, pp. 245103-245109, 2010.

[19] I. Koh, R. Hong, R. Weissleder and L. Josephson, "Sensitive NMR Sensors Detect Antibodies to Influenza," *Angewandte Chemie International Edition,* vol. 47, no. 22, pp. 4119-4121, 2008.

[20] T. J. Lowery, R. Palazzolo, S. M. Wong, P. J. Prado and S. Taktak, "Single-Coil, Multisample, Proton Relaxation Method for Magnetic Relaxation Switch Assays," *Analytical Chemistry,* vol. 80, no. 4, pp. 1118-1123, 2008.

[21] L. Josephson, J. M. Perez and R. Weissleder, "Magnetic Nanosensors for the Detection of Oligonucleotide Sequences," *Angewandte Chemie,* vol. 113, no. 17, pp. 3304-3306, 2001.

[22] D. Kim, M. K. Yu, T. S. Lee, J. J. Park, Y. Y. Jeong and S. Jon, "Amphiphilic polymer-coated hybrid nanoparticles as CT/MRI dual contrast agents," *Nanotechnology,* vol. 22, no. 15, p. 155101, 2011.

[23] D. M. Ghesani and D. C. R. Goldfarb, *General MRI.*

[24] C. Massin, F. Vincent, A. Homsy, K. Ehrmann, G. Boero, P.-A. Besse, A. Daridon, E. Verpoorte, N. de Rooij and R. Popovic, "Planar microcoil-based microfluidic NMR probes," *Journal of Magnetic Resonance,* vol. 164, no. 2, pp. 242-255, 2003.

[25] D. M. Puddephat, *Principles of magnetic resonance imaging,* 2010.